Automatic Feature Detection and Interpretation in Borehole Data

Thesis submitted in accordance with the requirements of

the University of Liverpool for the degree of Doctor in Philosophy

by

Waleed Tayseer Al-Sit

June 2015

Abstract

Detailed characterisation of the structure of subsurface fractures is greatly facilitated by digital borehole logging instruments, however, the interpretation of which is typically time-consuming and labour-intensive. Despite recent advances towards autonomy and automation, the final interpretation remains heavily dependent on the skill, experience, alertness and consistency of a human operator. Existing computational tools fail to detect layers between rocks that do not exhibit distinct fracture boundaries, and often struggle characterising cross-cutting layers and partial fractures. This research proposes a novel approach to the characterisation of planar rock discontinuities from digital images of borehole logs by using visual texture segmentation and pattern recognition techniques with an iterative adaptation of the Hough transform. This approach has successfully detected non-distinct, partial, distorted and steep fractures and layers in a fully automated fashion and at a relatively low computational cost.

Borehole geometry or breakouts (e.g. borehole wall elongation or compression) and imaging tool decentralisation problem affect fracture characterisation and the quality of extracted geological parameters. This research presents a novel approach to the characterisation of distorted fracture in deformed borehole geometry by using least square ellipse fitting and modified Hough transform. This approach approach has successfully detected distorted fractures in deformed borehole geometry using simulated data.

To increase the fracture detection accuracy, this research uses multi-sensor data combination by combining extracted edges from different borehole data. This approach has successfully increased true positive detection rate.

Performance of the developed algorithms and the results of their application have been promising in terms of speed, accuracy and consistency when compared to manual interpretation by an expert operator. It is highly anticipated that the findings of this research will increase significantly the reliance on automatic interpretation.

To my

Dear father and mother

Lovely wife and son

Great brother

and

Wonderful sisters

Acknowledgement

Contents

List of Figures

Chapter 1

Introduction

1.1   Background

Borehole imaging enables geophysicists to characterise subsurface conditions in considerable detail, detailing lithologic and groundwater flow conditions and identifying fractures, faults, layers and veins within the subsurface rock strata, facilitating the characterisation of intrusions for mining and geotechnical assessments. Such subsurface surveys require multi-sensor logging instrumentation to measure the fracture and bedding-plane dip and dip angle [9].

Borehole imaging tools provide an image for the borehole wall based on physical property contrast for the rock as shown in Figure 1.1. Nowadays, there is a wide range of imaging tools, these fall into three categories: optical, acoustic and resistivity. In mining geology, image logs are digital images acquired by a logging tool within a borehole. They represent measurements of the rock formation taken to the wellbore surface. Borehole imaging provides a high resolution images of borehole wall that contain information about layer properties, fractures and sedimentary structures. Interpretation of borehole data provides geologists with important information in different sections especially in industrial environment,

Figure 1.1: Borehole top view [1]

i.e, exploration for oil and gas, water mining.

Data processing is intensively performed after each logging acquisition, even integrating information from other tools, to characterise the features in terms of type, shape, dip and dip direction. This process is usually done manually by the experts, and it is an intensely time consuming task, depending heavily on the skill, experience, alertness and consistency of the operator, and the interpretation of the large volumes of borehole data are extremely challenging and often presents as implementation bottleneck.

The recent methods that have been developed to facilitate data interpretation typically involve mathematical model or image processing resulting in an awkward and computational intensive system inapplicable for online processing and large volume of data.

This research proposes algorithms to automatically detect and characterise fractures and layers using data acquired from different borehole logging tools

(optical, ultrasonic and resistivity). In order to achieve this, a number of novel data manipulation and processing methods have been deployed to extract information from different logs type, and several visual texture approaches employing the wavelet and texture analysis have been used for fracture detection. In addition, it proposes algorithms to detect, characterise and correct a distorted fracture in non-circular borehole shape.

1.2   Borehole Fractures

Breakout theory was originally proposed by Bell [10] and Gough [7], based on the equations in [11, 12]. The borehole breakout method is an important indicator of horizontal stress orientation, particularly in seismic regions and at small and intermediate depths. Borehole breakouts are stress-induced elongations that commonly appear over large sections along a borehole. As a result, borehole breakouts may provide continuous information on the state of stress, and therefore reveal important information on the continuity of the stress field in the rock mass [13]. Borehole breakouts can be detected using standard geophysical logging tools that map the geometry of the borehole wall.

Borehole fractures are stress caused by the enlargements of the borehole cross-section [14,15]. When the material are removed form the subsurface after borehole drilling, it is no longer supporting the surrounding rock, this causes the stress become concentrated around borehole wall as shown in Figure 1.2, where σ_H and σ_h are the maximum and minimum horizontal stresses. Borehole fractures happen when the stresses around borehole exceed that required to cause compressive failure of the borehole wall [16, 17].

Borehole fractures are a key factor to provide a clear view of the underground
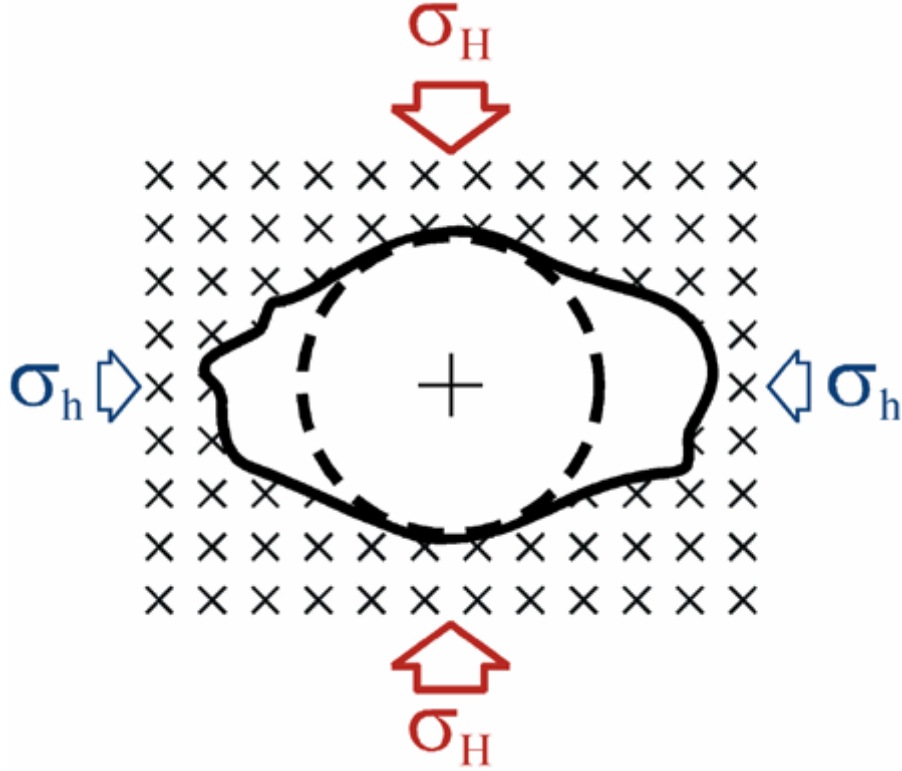
Figure 1.2: Graphical representation of stress-induced borehole breakout [2]

from geophysical point of view, it can help geologists to understand the stress situation around borehole wall and borehole stability. Fractures appear as sinusoids assuming the borehole to be cylindrical and are cutting by a planar fracture, as a result, the unwrapping image will show sinusoid as shown in Figure 1.3.

With reference to Figure 1.3, the dip direction with a cylindrical borehole is defined as the direction of the line formed by the intersection of a planar feature and a horizontal plane, while the dip angle gives the steepest angle of descent of a tilted bed or feature relative to a horizontal plane:

$$\text{dip angle} = \arctan(\hat{A}/r) \tag{1.1}$$

where $\hat{A}$ is the (scaled) sinusoid amplitude (in meters) and r is the borehole ra-
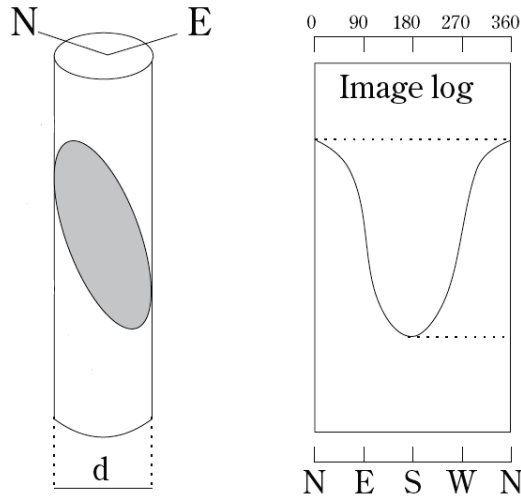
Figure 1.3: Illustration showing a planar feature intersecting a borehole and its typical sinusoidal appearance in the unwrapped presentation. (N, E, S, W) are the four directions

dius [18].

Borehole stability is weighted by fracture density (number of fractures in the well per unit well length). Failure in detecting the fracture correctly leads to [19]:

(i) increases the risk of drilling through fractured rock.

(ii) increases the probability of borehole collapse.

1.3 Previous Work

The standard approach for automated geological feature detection, i.e. computing an edge map and searching for sinusoids, has been widely applied in commercial borehole processing software. Thapa *et al* [18] proposed a semi-automated borehole log interpretation system based on the Hough transform. A 3D accumulator was constructed in parameter space to find the amplitude, phase and offset. The edge pixel candidates were selected according to the assumption that the geological feature pixels are darker than the rocks, so that the darkest 10% of the pixels in an image were chosen to contribute to the accumulator. The main drawback

of this method is the time consumption and the amount of memory needed for the three dimensional Hough transform to find the amplitude, phase and offset of sinusoidal waves. Taking the darkest 10% of the pixels to be geological features excludes a large category of geological features and this is a limitation. Glossop *et al* [20] used an algorithm similar to that by Thapa [18], the difference lies in the highlighting, which Glossop does using a Laplace-of-Gaussian filter.

Changchun [21] suggests an approach to reduce the complexity of Hough transform and decompose the problem of finding sinusoidal waves from 3D into 2D, thus reducing computational time and storage space. His algorithm is based on searching the midpoint that matched every pair of points in a fixed period. However, no experiments were conducted on real borehole images to verify this method.

Malone *et al* [22] proposed a system called the Borehole and Ice Feature Annotation (BIFA), providing the users with automatic or manual glacier borehole image annotation options. The automatic annotation algorithm is based on a modified version of the Canny edge detector to find edges based on intensity changes in the image; the user has the ability to customise Canny edge parameters, and after edges have been detected, the method of least squares is used to fit sinusoids onto edges in borehole images. For manual detection, the user has to select the highest and the lowest point of the edge, and the sinusoid is automatically detected.

He and Wang [23] proposed a method for rock fracture detection only using edge detection based on pulse coupled neural network (PCNN). The method was compared with well-known edge detection methods such as Canny edge detection and gradient methods. The result showed that the new method removes some

6

false edges but still contains noise and was only applied to one example, and the detected fractures were not characterised.

Wang *et al* [24] proposed a method based on edge detection and support vector machines (SVM). The proposed method is based on the concept of region detection using Canny edge detection to obtain a segmented image, then from the segmented image, 11 geometrical and statistical parameters were extracted to form the input vector to the classifier. The authors acknowledged that the proposed method did not achieve a good performance and without fracture characterisation results.

Johansson [25] proposed a method to extract and characterise fractures. The method is based on iterative intensity thresholding by extracting the darkest pixels in the image then the immediate neighbour pixels are included, this process is repeated until the fracture trace is filled. The fitting process is made as a method of least square fitting (LSF). The results showed that this method traces some fractures successfully but without fracture characterization results.

Ginkel *et al* [26] used a 3D generalised Radon transform to transform edge map into parameter space followed by post-processing to reduce the amount of incorrect picks by recomputing the Radon integral at all local maxima in parameter space and erase all points that support the curve from the orientation space. Their method was applied to resistivity borehole data and the authors acknowledged that the performance is at the expense of a considerable computational burden.

Assous *et al* [27] proposed a method to extract and characterise fractures in resistivity borehole images based on the combination of gradient based edge de-

tection and phase congruency implemented using Log Gabor wavelets to validate detected edges followed by sinusoid detection and 2D accumulator for sinusoid estimation. The authors claimed a false positive rate between 2% and 5% for resistivity data, with a computationally-efficient algorithm.

The borehole images suffer from a number of distortions, most of which can be identified as follows:

(a) Imperfect sinusoids due to:

    (i) Variations in the speed of the tool.

    (ii) The borehole is not perfectly cylindrical.

    (iii) The fracture is not perfectly planar.

(b) Partial sinusoids due to:

    (i) Missing data due to the partial coverage.

    (ii) True partial fractures (either through cementation or drilling induced fractures).

(c) Structures other than fractures introduced by some of the effects above, especially the partial coverage and the speed variations.

Most published experiments have been performed in boreholes with very well defined features and low levels of noise, which are not always representative of real geological data when related, for example, to complex depositional environment and field of stress or even dealing with rough borehole walls, impurities in the fluid or drilling-induced scratches. The existing algorithms are generally unable to detect non-distinct rock layers.

Fracture shape and parameters are directly related to the actual borehole geometries, it appears as an ideal sinusoid if it is assumed that the borehole is cylindrical and is cutting by a planar fracture. However, when the imaging tool is decentralised, or the borehole wall is elongated or compressed, the fracture appears as a distorted sinusoid, and provides non-meaningful geological parameters (i.e. dip and dip direction). Knowing the borehole geometry and dimensions will help to detect the fractures accurately.

In order to overcome the limitations of the current borehole image interpretation and annotation systems, a new scheme for geological features detection in borehole images based on multi-resolution texture segmentation and pattern recognition techniques is proposed to reduce human interaction with the interpretation process so as to be fully automated. The combination of visual texture segmentation and iterative use of the modified 2D Hough transform results in reducing the false peak detection, as well as enhancing the overall method accuracy. Enhancing automated detection accuracy reduces human involvement in the final result. The proposed method provides a non-subjective and accurate computer-based detection system for eminent borehole fractures. The block diagram of the proposed method is summarised in Figure 1.4.

The proposed method consists of the following steps:

(i) Borehole data is pre-processed in order to remove noise and clutters

(ii) Borehole characterisation using travel-time acoustic data.

(iii) Features extraction based on visual texture.

(iv) Modified Hubert (MH) index for number of cluster determination.

(v) Image segmentation using unsupervised classification.
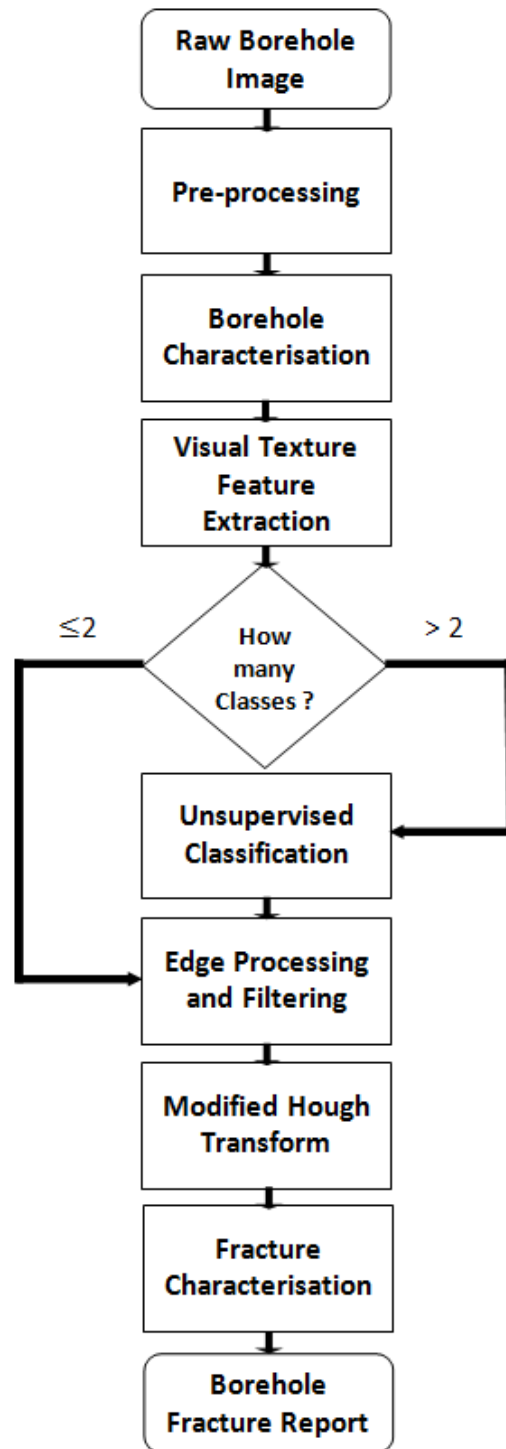
Figure 1.4: Block diagram of the proposed fracture detection method

(vi) Edge detection based on modified Canny edge detection.

(vii) Fracture detection and characterisation using modified Hough Transform(HT).

Moreover, to solve the problem of detecting distorted fracture shape form decentralised borehole data or breakout borehole, a new method based on non-linear least squares ellipse fitting to find the actual borehole geometry is proposed, followed by a modified version of Hough transform to detect and characterise the distorted fracture in deformed borehole. The proposed method successfully obtains accurate fracture parameters from non-circular borehole shape.

1.4   Aims and Research Objectives

This study addresses some of the issues outlined above, by adopting and developing a range of signal and image processing techniques from other disciplines into a comprehensive automated geological features that can be used effectively by untrained operator. The goal is to develop and apply the techniques necessary to provide automated borehole interpretation report without the requirement for extensive processing by the human operator. The particular anomaly types that this research is considering are:

(i) Rock layers that separated two different rock types.

(ii) Fractures and cross-layer that represent faults and breaks in the borehole wall.

The completed system processes different borehole log types, i.e; optical, acoustic and resistivity, to detect and characterise geological features indicating its dip and direction information. This information is required to be accurate and prompt. The requirements need a high degree of automation, and robustness computational efficiency.

1.5 Thesis Structure

This thesis is structured as follows: Chapter 2 describes the operation of various types of borehole imaging system and the data acquisition process and the pre-processing stages that prepare data for interpretation. Chapter 3 presents visual textures analysis to discriminate the geological features, while Chapter 4 presents edge detection techniques and fractures characterisation. Chapter 5 presents distorted fracture detection in deformed borehole shape, and multi-sensor data combination techniques that used to aggregate different borehole logs in order to enhance the overall system detection accuracy. Chapter 6 concludes the research by highlighting the achievements made to meet the objectives, pointing out the shortcomings and discussing the future research.

1.6 Contribution

The main contributions of the research work described in this thesis are:

(i) Proposed method to detect and characterise non-distinct, cross-cutting, partial fractures, high angle and disjointed fractures and layers from different types of borehole data, based on visual texture segmentation. The method proves to be accurate and non-subjective.

(ii) Proposed method for borehole shape modelling and automatic distorted fracture detection in deformed borehole geometry using acoustic borehole data. The proposed method is based on non-linear ellipse fitting and adaptive Hough transform, and detects distorted fracture shape and parameters accurately.

(iii) Proposed method for fracture detection result enhancement by using multi-sensor data combination techniques.

1.7 Published Work

W. Al-Sit, W. Al-Nuaimy, M. Marelli, and A. Al-Ataby, "Visual texture for automated characterisation of geological features in borehole televiewer imagery," Journal of Applied Geophysics, vol. 119, no. 0, pp. 139-146, 2015.

Chapter 2

Data Acquisition and
Pre-Processing

2.1 Introduction

Borehole scanner tools which measure physical properties in different directions
in a borehole allow to derive the directional dependence of rock properties in the
case of anisotropic formations (e.g., crystals, cracks, pores, layers or inclusions).
Among the scanner tools, borehole image tools produce images of the borehole
wall which are influenced by the surface of the borehole wall or a very small
depth of penetration of only a few millimetres. One fascinating aspect of these
image tools is that the data obtained can be presented on a computer like a core.
Then, it is possible to display and interpret on screen these virtual core images
with the associated virtual optical images of real cores created by an optical core
scanner [28].

Borehole Imaging tools provide an image for the borehole wall based on phys-
ical property contrast for the rock. Nowadays, there are a wide range of imaging
tools, these fall into three categories: optical, acoustic and resistivity, detailed

illustration of each method will be presented in the next sections. All methods utilise a built-in flux-gate magnetometer to orient the image with respect to magnetic north. The resulting data offers a unique ability to present the core as unwrapped image. Further analysis allows data to be presented in terms of depth, dip and direction of dip (with respect to North).

This chapter presents the data acquisition operation of various type of borehole imaging tools, particularly, optical, acoustic and resistivity. In addition, the various stages of pre-processing techniques to prepare the data for subsequent fracture detection and characterisation.

2.1.1   Optical Imaging

The optical televiewer offers a big advantage and attraction for geologists since it images the natural rock colours, it is like seeing the actual core. The optical televiewer requires clear fluid, or an empty, clean borehole.

The probe (as shown in Figure 2.1) uses a high resolution downward-looking camera with specific optic (a conical mirror with a ring of bulbs) with just one shot needed to capture the entire borehole circumference as a 360° panoramic view. Settings similar to traditional cameras (exposure, quality, light, frame rate, number of pixels) make it effective in almost clear type of borehole fluid. After each shot, a series of horizontal strings of pixels are acquired giving a rasterized RGB picture in real-time as transmitted to the console and finally to a PC monitor [3].

Optical borehole images represent the unfolded picture of borehole side walls, with the horizontal axis representing the bearing and the vertical axis the depth. Any intersection between dipping plane and a borehole is represented as different thickness of a sinusoidal strip, the image pixels values inside the strip are different

Figure 2.1: Optical televiewer probe [3]

from those of the surrounding formation [29, 30].

The orientation device embedded in the tool, made of 3 inclinometers and 3 magnetometers, allows inclination and azimuth of the borehole to be computed in real-time, thus automatically orientated images are rendered at convenient logging speed (typically in the 1-10 meters/minute range) [3].

Different borehole optical images were analysed and recorded using the HiOPTV probe from Robertson Geologging Ltd in 10-15 cm diameter boreholes. Mainly, volcanic formations were logged, with typically 1-2 mm vertical resolution (rows of pixels) and comparable horizontal detail (televiewer specifications are presented in Appendix B). An example section is presented in Figures 2.2 where the vertical axis is depth and horizontally is the borehole circumference always oriented starting from Magnetic North (left side of the image). Fracture and layer are appearing in Figure 2.2.

2.1.2 Acoustic Imaging

High-resolution Acoustic Televiewer (HiRAT) provides high-resolution, oriented images of the borehole walls presented in *pseudo-colour*. The probe uses a fixed
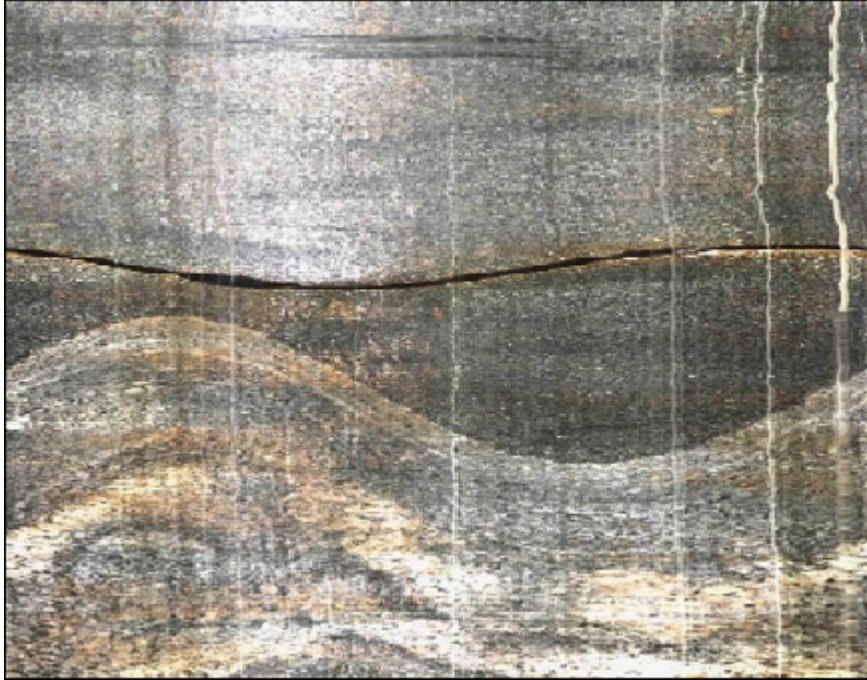
Figure 2.2: Optical televiewer borehole logs sample

acoustic transducer and a rotating acoustic mirror to scan the borehole walls with a focused ultrasound beam. The amplitude and travel time of the reflected acoustic signal are recorded simultaneously as separate image logs. Features such as fractures reduce the reflected amplitude and often appear as dark sinusoid traces on the log. The travel-time log is equivalent to a high-precision 360-arm calliper and shows diameter changes within open fractures and break-outs. Directional information is also recorded and used to orient the images in real time [4]. An example section of acoustic borehole log is shown in Figure 2.3.

High resolution acoustic pulses -1.5 MHz frequency- are generated by a fixed piezo-electric resonator and then transmitted along the tool axis to be reflected by a rotating planar mirror as shown in Figure 2.4. The beam is ultra-focused to achieve highest resolution. After mirror reflection, the pulses propagate orthogonally to the probe body through the acoustic window (nylon construction for acoustic impedance) then through the borehole fluid to be reflected by the
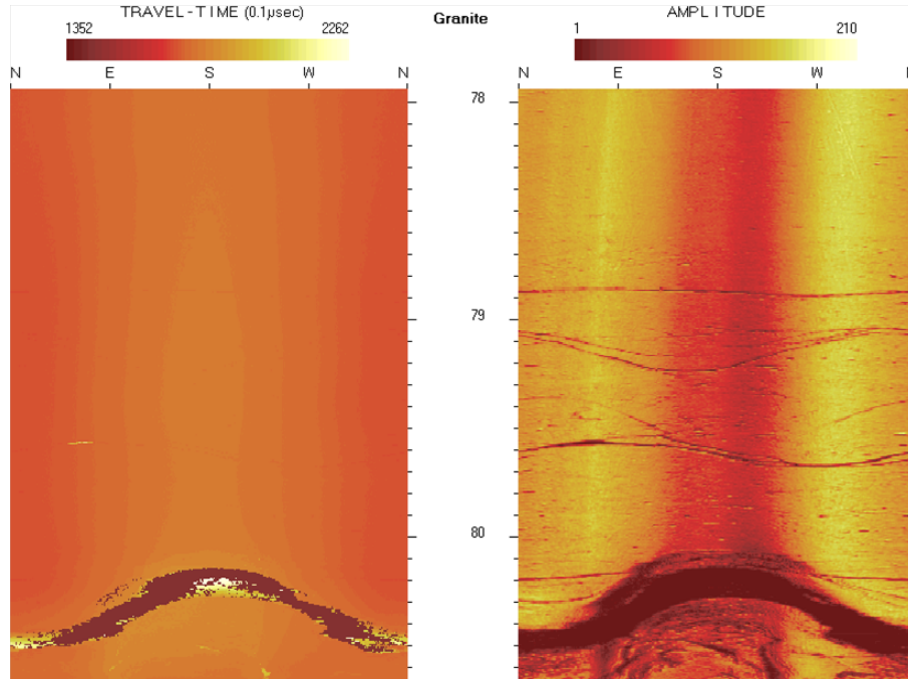
Figure 2.3: Acoustic borehole log [4]

wall of the borehole following an almost normal incidence. The reflected energy
is automatically picked up by the same transducer, in a reverse path, from which
the amplitude of the returned first reflections and the related elapsed two-way
travel time are recorded.

Typical logging speed is in the $1.5 - 5$ m/minute range (to be constant). High
vertical and horizontal resolution (i.e. 360 samples per rev) requires slow logging
speed. Logging too fast will result in incomplete borehole wall imaging (lack of
vertical resolution) with the resulting plots appearing compressed in the acquisi-
tion software. On the other side, logging excessively slowly does not result in a
better image, it only increases redundancy in the data stream and hence the stor-
age requirement. This is because any horizontal point might be imaged by more
than one sweep of the acoustic beam (according to head speed and baud rate [4]).

Unlike the optical televiewer, the acoustic televiewer can be run in both clear
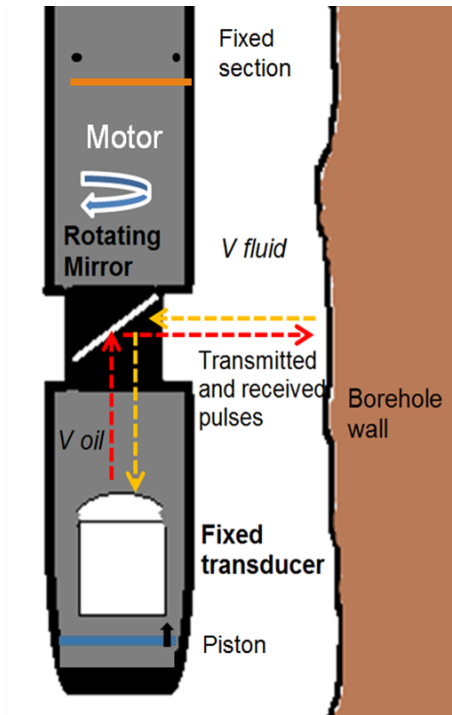
Figure 2.4: Illustration of acoustic acquisition tool [4]

and opaque mud. The acoustic televiewer is more reliable for a wider variety of applications, because it is often easier to use mud to keep fluid in the hole than to either flush the hole clean, or empty it, or wait until the fluid clears up. Further, the HiRAT can more easily detect the fine fractures [4].

2.1.3 Resistivity Imaging

The resistivity borehole imager, also called (Formation Micro Imaging FMI), was developed for the oil market and is still mainly used there [31]. The resistivity imaging have developed gradually from dip-meter tools and typically consist of four to six arms with one or two conductivity pads attached that contain a number of resistivity buttons at the end of each arm. The pads are pressed against borehole wall to measure the formation micro-conductivity [31] producing an electrical image of the borehole.

Resistivity image tool is widely used in exploration due to it is structure sim-

plicity, low cost of equipments and ease of use. FMI provides detailed information of layers formations, identification of structural geology, fractures and rock textures [32].

The resistive FMI tool takes continuous circumferential micro-conductivity measurements in the borehole, producing an electrical image of the borehole, oriented with respect to North by means of a gyroscopic compass [31,32]. Data are processed and displayed as either a static (data equalised over the entire depth range of the logging run) or dynamic equalisation (data equalised over a much shorter window, usually 510 m), unrolled inside wall image, clockwise from 0° (North) to 360°.

In this research a resistivity imaging tool form Roberson Geologging Ltd is used. The tool includes 4 pads each containing twelve button electrodes mounted on 2 pairs of powered arms [33]. Resistivity borehole data sample is shown in Figure 2.5. In general yellow colours in resistivity log represents more resistive rock type.

2.2 Data Pre-Processing

Pre-processing is an essential step in order to prepare collected borehole data for subsequent processing. It is found that data pre-processing has a key role when trying to build an automated interpretation system using computer algorithm. The environment of drilled borehole (e.g. when borehole is flushed by a clear fluid or it is full of mud) and the configuration of data acquisition system may introduce a host of errors that can't be accounted by manual interpretation. This leading to degradation of the quality of the acquired borehole data, influencing the robustness of any automatic interpretation system as it needs a high quality image
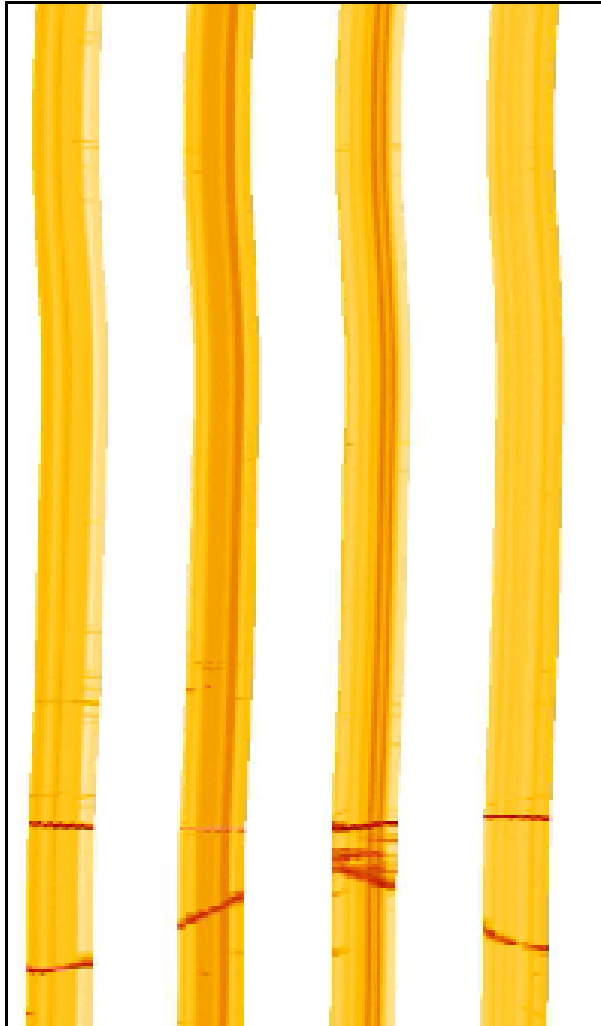
Figure 2.5: Resistivity log sample

with non-masked fracture. A series of pre-processing techniques including median filtering, sub-sampling, decentralisation compensation and histogram equalisation are performed in order to enhance the image quality. Due to the length of the borehole image that varies from a few meters to hundreds of meters, the image is partitioned into smaller parts in order to ease the processing.

2.2.1   Background Removal

Borehole image noise and clutter can be caused by the probe decentralisation problem, the well is not cleaned very well after drilling process or the tool has a stick/slip behaviour which is often due to varying well diameter. The clutter appears as vertical stripes or affect contrast quality of borehole data, and thus it will affect the feature extraction and characterisation. Figure 2.6(a) shows an example a poorly centralised acoustic sensor that appear as two parallel vertical strips.

It is possible to remove background or clutter by subtracting from the borehole data an ensemble average of the borehole data image over the region of interest. Here it is assumed that the target indication are present in a relatively small number of measurements and the mean of borehole data can be considered to be a measure of system clutter. The image is divided into horizontal lines and then the ensemble mean of each column of pixels intensities across each strip is subtracted. Assume the unprocessed image y and win the size of strip starting from point j_{bg}, the processed image $\hat{y}(i)$ is calculated using

$$\hat{y}(i) = y(i) - \frac{1}{win} \sum_{j=j_{bg}}^{j_{bg}+win-1} y(j) \qquad (2.1)$$

Image clutter may be removed by specifying the corresponding values of j_{bg} and win. Figure 2.6(b) shows how this technique remove background noise. This
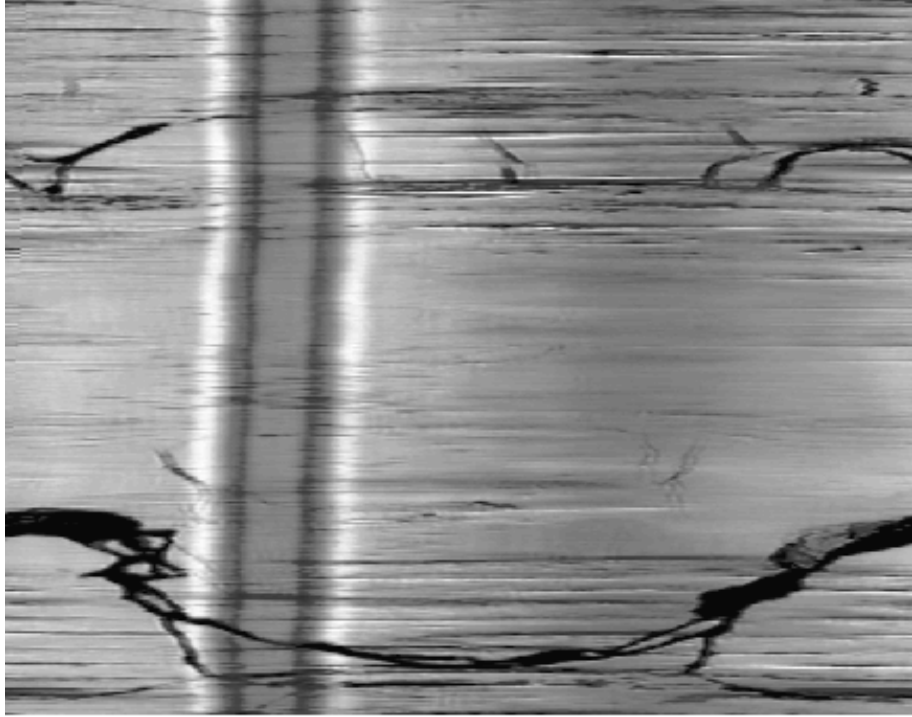
(a) Acoustic amplitude image, before background removal
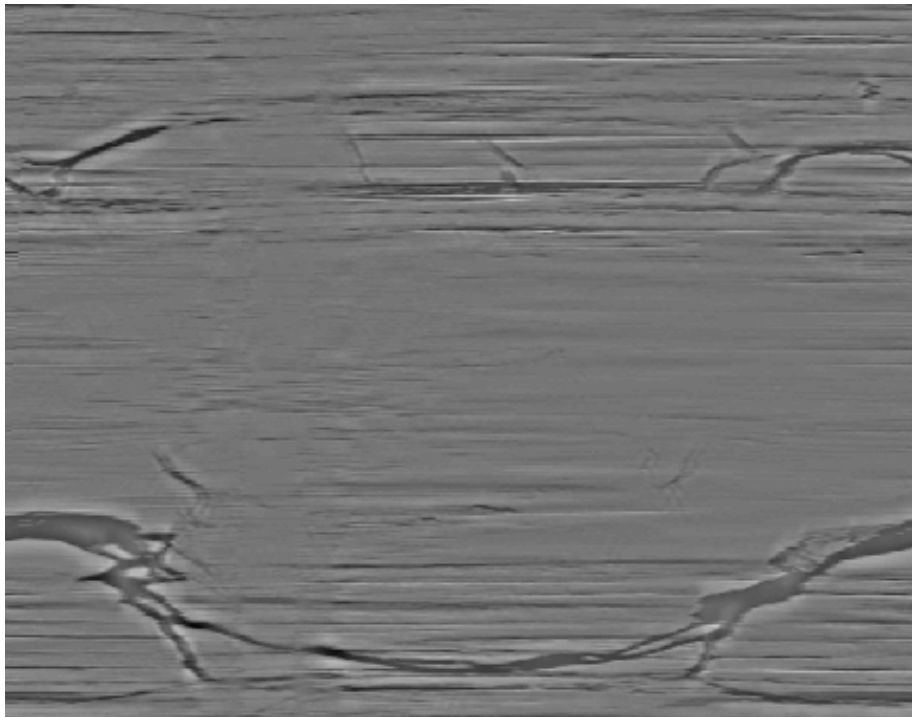
(b) Acoustic amplitude image, after background removal

Figure 2.6: Contrast-enhancement caused by background removal

technique is particularly well-suited for instances where the fractures are well-separated from system clutter, and affects on thin fractures detection accuracy.

2.2.2   Probe Decentralisation Correction

Detailed information about the borehole shape can be derived from the acoustic travel-time image. As discussed in Section 2.1.2, the acoustic tool does not really measure borehole calliper (continuous measurement of the size and shape of a borehole along its depth) rather it measures multiple distances from the tool to the borehole wall. Calliper is only defined with respect to the centre of a regular shaped borehole.

Probe centralisation is fundamental to have high quality images, Robertson Geologging Ltd brass centralisers work on the bowstring principle, with three or four arms (depending upon the diameter and centralisation force required).

However, probe decentralisation affect on collected data. In Figure 2.7 three different situation are schematically presented. In case 1, the tool is decentralised in a circular borehole. The two green arrows indicate the two directions where the acoustic beam hits the borehole wall perpendicularly. Only at these two directions give maximum reflection amplitudes and the addition of the two opposite travel-times gives the true borehole calliper. In the direction of the two red arrows we measure a secant. The length of the secant depends on tool position. in case 2, the beam is perpendicular to the borehole wall in four directions. Calliper values can be calculated in all directions, because the tool is in the centre of the borehole cross-section. In case 3, the tool is decentralised in an elliptical borehole. The borehole wall is hit perpendicularly in four directions. But it is quite obvious that the addition of the distance given by the red arrows and distance in the opposite direction (green arrow) does not give a meaningful calliper value.
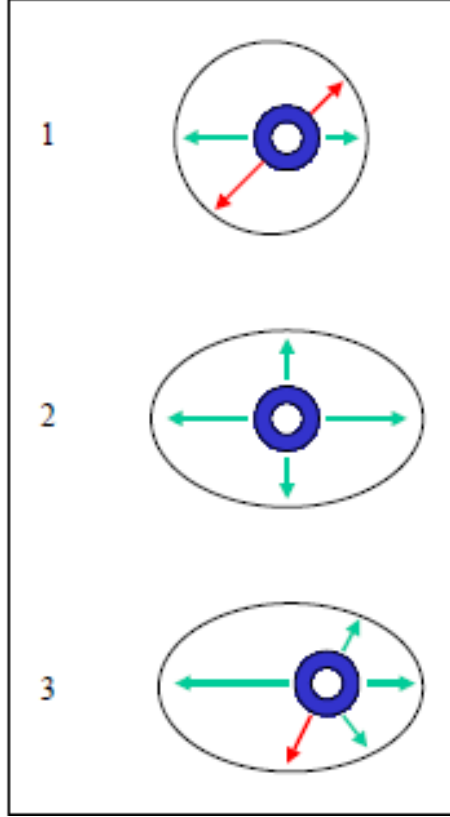
Figure 2.7: Probe decentralisation cases

To overcome probe decentralisation problem, the borehole shape should be detected by mapping the travel-time data into distance data (y,x) relative to the centre of the borehole in terms of radius (r) and angle (ϕ). This gives the possibility to accurately detect the movement of the tool from its actual position to the centre of the borehole. Then proposed ellipse fitting process is performed by using non-linear least squares function to find the borehole dimension. This will be discussed in detail in Section 5.1.

2.3   Summary

This chapter has described different method for borehole data acquisition, these methods include optical, acoustic and resistivity. For each method, the acquisi-

tion parameters, environment and data sample were presented.

Moreover, the pre-processing methods were presented to prepare the borehole data in a format suitable for subsequent processing. The pre-processing include background removal which enhances borehole data contrast, and solving of probe decentralisation problem which affects borehole data readability. This prepares the data in a format suitable for further processing and feature detection.

Chapter 3

Visual Texture and Image Segmentation

3.1   Introduction

In previous chapter borehole data is pre-processed and prepared for further processing and feature detection. Due to the noisy nature of borehole data, the main challenge is to find the texture boundaries even if the textured surface cannot be classified, this problem can be solved using texture segmentation to obtain a map of boundaries of similarity-textured regions. Defining texture boundaries helps in extracting smooth edges in the next step of the proposed method (edge detection) as shown in Figure 1.4.

Texture analysis methods have been utilised in a variety of application domains. In some of the similar domains (such as remote sensing) texture already has played a major role. In order to segment an image, it is important to extract meaningful features that represent each segment accurately to enable segregation of the distinctive regions contained in the image. Visual texture is one of the most important features that allows distinguishing different image objects or

surfaces with similar shape or colour. Texture, although recognised when seen, is very difficult to define. This difficulty means that a single, unambiguous and widely accepted definition does not exist. A reason for this is the strong intuitive concepts of texture, which are hard to encompass fully in a formal definition.

3.2 Texture Properties

Texture can be recognised when seen but it is very difficult to define. This difficulty is demonstrated by the number of different texture definitions attempted by vision researchers [34, 35]. Coggins [36] has compiled a catalogue of texture definitions in the computer vision literature as listed below [37]:

"A region in an image has a constant texture if a set of local statistics or other local properties of the picture function are constant, or approximately periodic." [38]

"The image texture we consider is non-figurative and cellular... An image texture is described by the number and types of its (tonal) primitives and the spatial organisation or layout of its (tonal) primitives... A fundamental characteristic of texture: it cannot be analysed without a frame of reference of tonal primitive being stated or implied. For any smooth gray-tone surface, there exists a scale such that when the surface is examined, it has no texture. Then as resolution increases, it takes on a fine texture and then a coarse texture." [39, 40]

This collection of definitions demonstrates that the definition of texture is formulated by different people depending upon the particular application and that there is no generally agreed upon definition. Image texture, defined as a function of the spatial variation in pixel intensities (gray values), is useful in a variety of
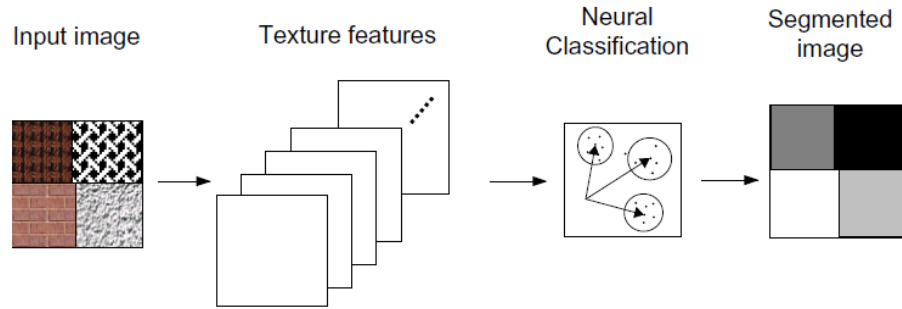
Figure 3.1: Processing stages of texture segmentation system

applications. Defining homogeneous regions in an image is the most important application in visual texture and is called *texture classification*. The goal of texture classification is to produce a classification map of the input image where each uniform textured region is identified with the texture class it belongs to [34, 41]. The second type of problems that texture analysis research attempts to solve is to find the texture boundaries even if we could not classify these textured surfaces and its called *texture segmentation*, the goal of texture segmentation is to obtain the boundary map of homogeneous regions.

The stages of the segmentation technique adopted here are outlined in Figure 3.1. A segmentation is produced by integrating different texture features. If the texture features (to be described below) are capable of discriminating these categories then the patterns belonging to each category will form a cluster in the feature space which is compact and isolated from clusters corresponding to other texture categories. The recovery, discrimination and labelling of such clusters is performed by neural networks [5].

3.3 Texture Analysis Techniques

As there are a wide range of definitions, applications and concepts relating to texture analysis, this has led to a wide range of methods for detecting and inter-

preting texture. These methods can be broadly categorised into four classes:

1. **Structural methods**: they consider textures to have two fundamental components: a basic primitive (called a texel) that comprises the texture and the spatial organisation of these primitives. Since this only allows the description of very regular textures, the rules are often extended to become statistical, which offers more freedom in the description [42]. The advantage of the structural approach is that it provides a good symbolic description of the image; however, this feature is more useful for synthesis than analysis tasks.

2. **Statistical methods**: they do not attempt to understand explicitly the hierarchical structure of the texture. Instead, they represent the texture indirectly by the non-deterministic properties that govern the distributions and relationships between the grey levels of an image. These can be first-order statistics (e.g. mean and histogram) and higher order statistics mostly second-order. Gray-level-co-occurrence matrix is the most popular statistical method which proposed by Haralick [43].

3. **Model-based methods**: they attempt to characterise textures by constructing a stochastic model, this can be done by fitting some analytical function to the texture. In practice, the computational complexity arising in the estimation of stochastic model parameters is the primary problem. Gibs-Markov, Random filed and auto-regressive models are typical examples of these methods [44, 45].

4. **Transform methods**: represent the image into something more meaningful or in a new form in which textures can be detected more easily. Multiresolution methods are typical of these that transform images into a new representation which separates features of different scale and resolution, and provide texture spatial localisation.

According to the need of finding homogeneous regions in borehole data, and extract non-distinct fracture and layers, which are located between different regions at acceptable computational complexity. This research concentrate on statistical and multi-resolution methods, and investigate their applications in borehole data characterisation.

3.4 Statistical Texture

Statistical texture analysis computes local features at each point in a textured image, and derives a set of statistics from the distributions of the local features. The local feature is defined by the combinations of intensities at specified positions relative to each point in the image. According to the number of points which define the local feature, statistics are classified into first-order, second-order, and higher order statistics [46]. The pioneering work of Julesz [47] concentrated on these spatial statistic properties of the image gray levels [48].

The basic difference between first-order statistics and higher-order statistics is that first-order statistics estimate properties (e.g.average and variance) of individual pixel values, ignoring the spatial interaction between image pixels, while second and higher-order statistics estimate properties of two or more pixel values occurring at specific locations relative to each other.

3.4.1 First-order Statistics

First-order statistics measure the likelihood of observing a gray value at a randomly chosen location in the image. First-order statistics can be computed from the histogram of pixel intensities in the image, these depend only on individual pixel values and not on the interaction or co-occurrence of neighbouring pixel values. The average intensity in an image is an example of the first-order statistic.

Assume a two-dimensional image function discretised into gray levels. The occurrence probability of intensity i in the image is given by:

$$h(i) = \frac{\theta(i)}{A} \qquad (3.1)$$

where $\theta(i)$ $(i = 1, 2, \ldots, g)$ is the number of points whose intensity is i in the image and A is the area of the image (the total number of pixels in the image).

This distribution takes the form of a histogram. The histogram function is computed for small, overlapping region and resulting distribution associated with the centre pixel of the region because different image partition may have different textures.

The following are the simple seven first-order texture measures that are often used to characterise the histogram: **mean**, **variance**, **skewness**, **kurtosis**, **fifth moment**, **histogram entropy** and **relative smoothness**, are calculated as follows:

1. Mean:

$$\mu_h = \sum_{i=1}^{g} i h(i) \qquad (3.2)$$

2. Variance (second moment)

$$\sigma_h^2 = \sum_{i=1}^{g} (i - \mu_h)^2 h(i) \qquad (3.3)$$

3. Skewness (third moment):

$$\sum_{i=1}^{g}(i - \mu_h)^3 h(i) \tag{3.4}$$

4. Kurtosis (fourth moment):

$$\sum_{i=1}^{g}(i - \mu_h)^4 h(i) \tag{3.5}$$

5. Fifth moment:

$$\sum_{i=1}^{g}(i - \mu_h)^5 h(i) \tag{3.6}$$

6. Histogram entropy:

$$-\sum_{i=1}^{g} h(i) \log h(i) \tag{3.7}$$

7. Relative smoothness:

$$1 - \frac{1}{1 + \sigma_h^2} \tag{3.8}$$

The distribution mean μ_h is not considered as an independent feature, as there is no observed correlation between it and the different texture categories, it is computed in order to compute the further features.

Each measure is a function of the pixel intensity distribution $h(i)$ within any $(N \times N)$ region centred at any arbitrary point (x, y). These square windows are shifted across the image in a small increment of size ϵ, where $(\epsilon \geq 1)$. This finite increment makes it necessary to associate the texture feature value with an $\epsilon \times \epsilon$ square centred around (x, y). The result of features matrices represent points that have some relationship to the probability distribution function of pixel intensities within its neighbourhood.

The finite window size will not cover the point in the vicinity of the image

(a) Image of a fingerprint

(b) After addition of border
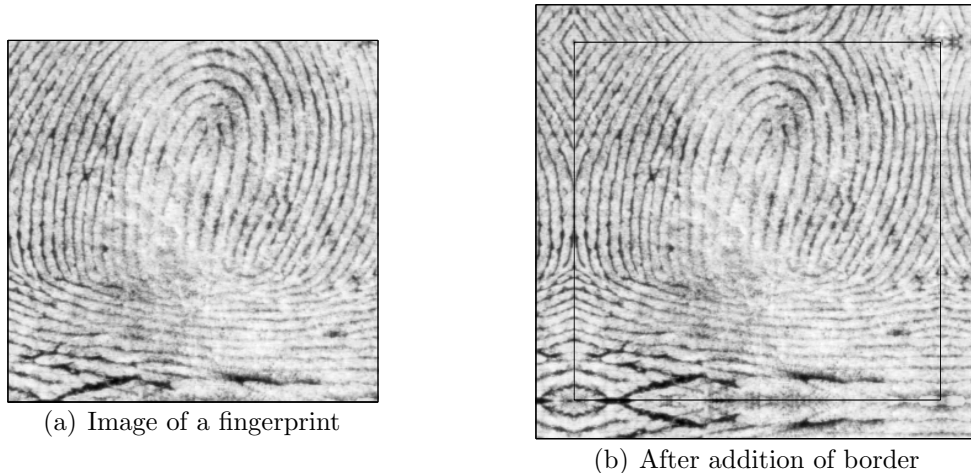
Figure 3.2: Example of the reflected image border to overcome the difficulty in computing boundary features

boundaries so these point will not be mapped. To overcome this problem, the image is surrounded with a reflected replica of the image border, of thickness $N/2$, as shown in Figure 3.2. A value of $N = 20$ was chosen in order to capture the variations in fracture amplitude, and a value of 5 was assigned to ϵ, resulting in 75% adjacent window overlap.

Although first-order statistics provide features descriptions, it might not be enough for the discrimination process. As demonstrated by Julesz [47], two textures could have identical first-order statistics, because these measures may not carry any information regarding the relative positions of pixels with respect to each other. This limitation can be overcome by using of of second-order statistics [48–50].

3.4.2 Second-order Statistics

Second-order co-occurrence texture features are defined as the likelihood of observing a pair of gray values occurring at the endpoints of a dipole (or needle) of random length placed in the image at a random location and orientation. These

are properties of pairs of pixel values. It was first introduced by Haralick [39, 43] in the seventies, and it was found that the co-occurrence features is the best with regards to texture classification performance for the experimental results that were presented in [51, 52].

Co-occurrence textural features are computed based on gray-tone spatial dependencies. Assuming a position operator $\Delta = (\Delta_x, \Delta_y)$, joint probability matrix P_Δ and joint probability of the existence of a pair of pixels with intensities i and j existing at separation Δ is denoted by $P_\Delta(i, j)$. P_Δ is called *gray level co-occurrence matrix* or simply **(GLCM)**, This matrix depends both on the angular relationship between pixels and the distance between them. Matrix manipulation allows the co-occurrence matrix to be computed in a fast and efficient manner.

For any particular position operator Δ one can define a large number of descriptors or features that characterise the or features that characterise the content of P_Δ. From the abundance of features available, previous studies(e.g. [51, 53]) recommend to use the following eight features [54]:

1. The maximum probability gives an indication of the strongest response to Δ:

$$max_{i,j} P_\Delta(i, j) \tag{3.9}$$

2. The element-difference third-order moment:

$$\sum_{i=1}^{g} \sum_{j=1}^{g} (i - j)^3 P_\Delta(i, j) \tag{3.10}$$

35

3. The inverse element-difference second-order moment:

$$\sum_{i=1}^{g}\sum_{j=1}^{g}\frac{P_\Delta(i,j)}{(i-j)^2} \quad (i \neq j) \tag{3.11}$$

4. Energy or the angular second moment, which is a measure of uniformity, and is alternatively referred to as inertia:

$$\sum P_\Delta(i,j)^2 \tag{3.12}$$

5. The correlation is a measure of linearity:

$$\frac{\sum_{i=1}^{g}\sum_{j=1}^{g}ijP_\Delta(i,j)^2 - \mu_x\mu_y}{\sigma_x\sigma_y} \tag{3.13}$$

where:

$$\mu_x = \sum_{i=1}^{g}i\sum_{j=1}^{g}P_\Delta(i,j) \tag{3.14}$$

$$\mu_y = \sum_{j=1}^{g}j\sum_{i=1}^{g}P_\Delta(i,j) \tag{3.15}$$

$$\sigma_x = \sum_{i=1}^{g}(i-\mu_x)^2\sum_{j=1}^{g}P_\Delta(i,j) \tag{3.16}$$

$$\sigma_y = \sum_{j=1}^{g}(j-\mu_y)^2\sum_{i=1}^{g}P_\Delta(i,j) \tag{3.17}$$

6. Entropy is a measure of randomness:

$$-\sum_{i=1}^{g}\sum_{j=1}^{g}P_\Delta(i,j)\log P_\Delta(i,j) \tag{3.18}$$

7. Homogeneity is defined as:

$$\sum_{i=1}^{g}\sum_{j=1}^{g} \frac{P_{\boldsymbol{\Delta}}(i,j)}{1+|i-j|^2} \qquad (i \neq j) \tag{3.19}$$

8. Contrast is a measure of the amount of local variations present in the image window:

$$\sum_{i=1}^{g}\sum_{j=1}^{g}(i-j)^2 \, P_{\boldsymbol{\Delta}}(i,j) \tag{3.20}$$

The above eight features when multiplied by the number of possible values of Δ for which the co-occurrence matrix can be computed leads to a potentially large number of dependent features. As there have been no clearly-established guidelines for the selection of Δ, the correct choice for this operator is usually achieved on a trial-and-error basis. A value of $(3,3)$ has been used in this study and has achieved satisfactory results with the borehole images in question. In addition to the eight features calculated above, a two-dimensional entropy measure has been utilised, because it has proven to be effective as texture feature as proposed in [55, 56].

The proposed histogram is a (gray-level/local average gray-level) $g \times g$ scatterplot, each bin of which is related to the frequency of occurrence of the particular (gray-level/average) pair within the 5×5 pixel window. The a priori-probability $h_2(i,j)$ of an intensity pair (i,j) is given by the total number of occurrences of the pair divided by the total number of pixels. The total entropy for this $2-d$ histogram is given by:

$$-\sum_{i=1}^{g}\sum_{j=1}^{g} h_2(i,j) \log h_2(i,j) \qquad (3.21)$$

The result are in a total of 15 statistical texture features images, these images are normalised to have zero mean and unity standard deviation. This avoids system bias to the large numerical range, then the images are stacked together in 3-dimensional matrix as in Figure 3.3. Each pixel in the original image is mapped into 15-element feature vector.
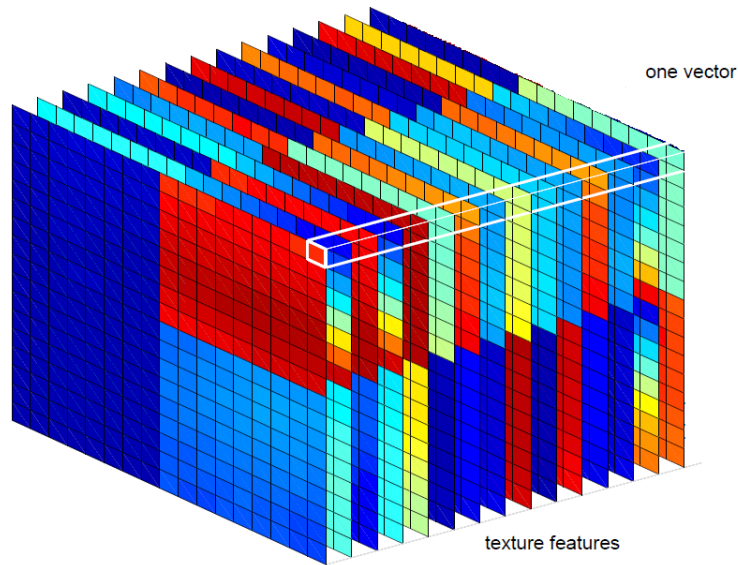
Figure 3.3: Formation of feature vector from feature images

The list below summarise the 15 statistical texture features image:

1. Histogram variance

2. Histogram skewness

3. Histogram kurtosis

4. Histogram fifth moment

5. Histogram relative smoothness

6. Histogram entropy

7. Co-occurrence correlation

8. Co-occurrence maximum probability

9. Co-occurrence third-order difference moment

10. Co-occurrence second-order inverse difference moment

11. Co-occurrence entropy

12. Co-occurrence uniformity

13. Co-occurrence contrast

14. Co-occurrence homogeneity

15. Two-dimensional entropy

3.5 Mutiresolution Texture

The approach adopted here is multi-channel filtering, and it is a more recent approach to texture analysis, inspired by multi-channel filtering theory for processing of visual information in the early stages of human visual system [57, 58]. Various cells within the visual cortex can perform different types of processing on the incoming signal. It has also been proven that the human visual system decomposes the retinal image into a number of filtered images, each image contains intensity variations over a narrow range of frequency and orientation [5].

A multi-channel filtering technique projects the image onto a set of two-dimensional Gabor filters, these filters are used as an approximate basis for a
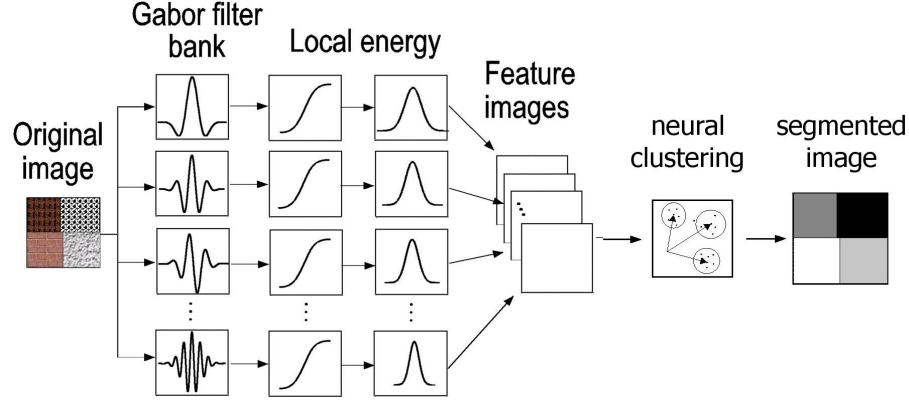
Figure 3.4: Stages of multi-resolution texture segmentation procedure

Wavelet transform. This generates a descriptor for each image pixel. Neural networks techniques are then used to segment the image as shown in Figure 3.4.

3.5.1   Gabor Filter

In their simplest form, Gabor functions are harmonic oscillations modulated by a Gaussian probability pulse. These elementary signals are localised in time and in frequency and possess the important property of minimising the combined effective spread in both time and frequency. Gabor signals have been proven [59] to provide dual space/spatial-frequency dependence simultaneously and model very well the spatially localised receptive field of visual cells [60].

A two-dimensional symmetric Gabor filter can be defined as a sinusoidal plane wave of some frequency and orientation modulated by a 2-D Gaussian envelope. The impulse response of a complex canonical Gabor filter in the spatial domain is given by:

$$g(\breve{x}, \breve{y}) = \frac{1}{\sqrt{2\pi\sigma_g}} \exp\left[-\frac{1}{2}\left(\frac{\breve{x}^2}{\sigma_x^2} + \frac{\breve{y}^2}{\sigma_y^2}\right)\right] . \cos\left(-2\pi u_0 \breve{x} + \rho\right) \qquad (3.22)$$

where u_0 and ρ are the frequency and phase of the sinusoidal plane wave, σ_x

and σ_y are the space constants of the Gaussian envelope along the x and y-axes respectively [61–63], and σ_g is equal to σ_x, σ_y and $\breve{x}$ and $\breve{y}$ are the oriented x and y co-ordinates after undergoing a rotation by an arbitrary angle α using Equation 3.24.

Selection of σ_x and σ_y determines the resolution in both spatial and spatial-frequency domains. Low values of σ_x and σ_y favour spatial resolution, and high values favour spatial-frequency resolution. When segmenting an image, short spatial intervals are preferable because one wishes to approximate the boundary between textures. However smaller frequency bandwidths are preferable to make better distinctions between different textures. The main challenge is the inverse relation between spatial-frequency and the spatial extent, this known by the uncertainty principle.

The Fourier spectrum of a Gabor function of radial frequency u_0 and orientation α is a pair of real-valued Gaussian, centred in the spatial-frequency domain at radial distances (proportional to) u_0 and $-u_0$ from the origin, and oriented at (an angle proportional to) the filter orientation α. When the phase is zero, the Fourier transform of the real component of the even-symmetric Gabor function $g(x, y)$ above is given by:

$$G(u,v) = 2\pi\sigma_x\sigma_y \left(\exp -\frac{1}{2}\left[\frac{(u-u_0)^2}{\sigma_u^2} + \frac{v^2}{\sigma_v^2}\right] + \exp -\frac{1}{2}\left[\frac{(u+u_0)^2}{\sigma_u^2} + \frac{v^2}{\sigma_v^2}\right] \right)$$

(3.23)

where $\sigma_u = \frac{1}{2\pi\sigma_x}$ and $\sigma_v = \frac{1}{2\pi\sigma_y}$, and $\breve{u}$ and $\breve{v}$ correspond to the spatial frequency co-ordinates u and v rotated by α, obtained as in Equation 3.24 by multiplying by the Givens matrix.

Table 3.1: Filter parameters for Gabor filter bank

Parameter	Filter number											
	1	2	3	4	5	6	7	8	9	10	11	12
σ_x/x_size	1	1	1	1	1	1	1	1	1	1	1	1
σ_y/y_size	1	1	1	1	1	1	1	1	1	1	1	1
u_0	1	1	1	1.5	1.5	2	2	2.5	2.5	3.5	3.5	3.5
α (°)	10	90	170	60	140	50	130	20	100	10	90	170
ρ (°)	0	0	0	0	0	0	0	0	0	0	0	0

$$\begin{pmatrix} \breve{x} \\ \breve{y} \end{pmatrix} = \begin{pmatrix} \cos\alpha & \sin\alpha \\ -\sin\alpha & \cos\alpha \end{pmatrix} \cdot \begin{pmatrix} x \\ y \end{pmatrix} \tag{3.24}$$

Hence,

$$\breve{x} = x\cos\alpha + y\sin\alpha \tag{3.25}$$

and

$$\breve{y} = -x\sin\alpha + y\cos\alpha \tag{3.26}$$

The illustration of the effects of varying the orientation of the filter on the corresponding spectra, radial frequency and Gaussian space constants are shown in Figure 3.5.

Various of filters are constructed and the configurations are summarised in Table 3.1, with the aim of a uniform coverage of the spatial-frequency plane. Filters were selected with orientations varying from 10° to 170° in steps of 20°, and with radial frequencies one octave apart from 1 to 8 cycles/image-width. Although this filter set comprising $9 \times 4 = 36$ filters gave satisfactory results, experimental variations were made on this initial set in order to reduce the number of filters and thus reduce the data and the processing time. It was observed that the low-frequency filters were more effective in distinguishing the required textures, and a modified filter set was composed, comprising of only 12 filters, and with frequencies ranging from 1 to 3.5.
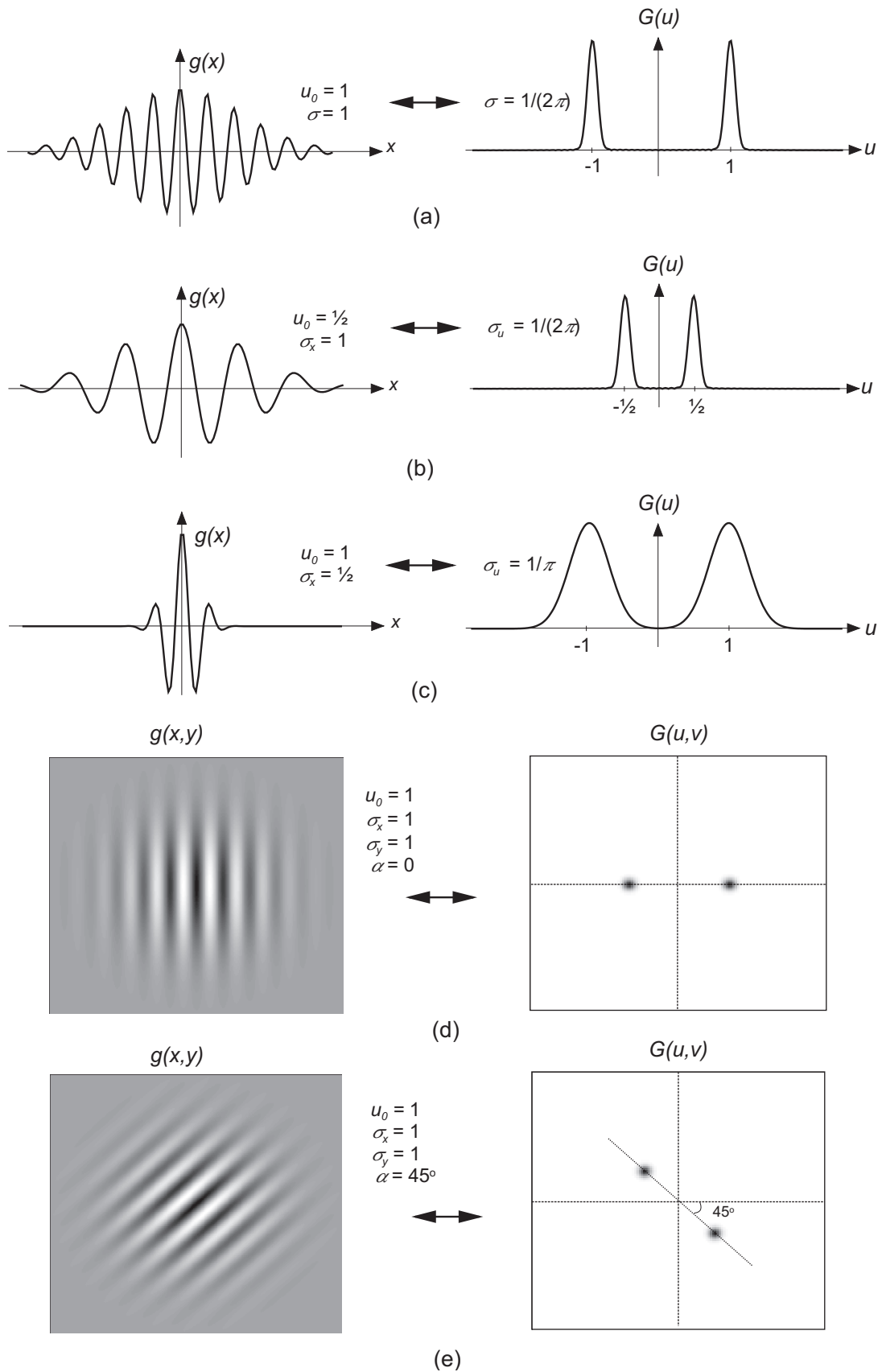
Figure 3.5: Graphical illustration of the effect of filter frequency (u_0), space constant (σ) and orientation (α) on the corresponding spectra [5]

3.5.2   Filtering

The filtering operation is performed in the spatial domain, by convolving each filter function $g_i(x, y)$ with the image $f(x, y)$ as follows:

$$h_i(x, y) = |g_i(x, y) * f(x, y)| \quad (i = 1, 2, \ldots, 12) \tag{3.27}$$

Each pixels magnitude reveals the relative strength of the variations characterised by the filter attributes in its neighbourhood in the original image. Since these filters have the property of achieving the optimum localisation in both domains, each filtered image shows the best possible distribution of the spatial signals within the given bandwidths of the corresponding filter.

The filtering operation results in a set of 12 independent 256×256 filtered images, stored in a 3-dimensional matrix. In order to keep the intensities of the outputs from all the filters within a common range, each image was then normalised to have zero mean and unity standard deviation.

3.5.3   Feature Computation

Before segmentation can be performed, a set of texture measures or features must be developed from these filtered images. As suggested in [64], attributes of blobs in these images can be captured by applying a non-linear transformation in order to transform the sinusoidal modulations to square modulations. The non-linearity employed is the hyperbolic tangent as suggested in [65]. This blob image can then be analysed and local measures computed and used as features. The local energy is used as a texture feature as suggested in [5], generating one feature image per filter, resulting in F feature images for the present filter set. This local energy is computed by convolving the filtered images with a 2-dimensional $m \times n$ Gaussian-weighted window whose space constant σ_ω is proportional to the average size of

44

intensity variations in the image, which is in turn related to the Gabor filter centre frequency u_0 as in [66]:

$$\sigma_\omega = \frac{\kappa_\omega}{u_0} \tag{3.28}$$

where the constant κ_ω is chosen (empirically) as 0.5 image-widths/cycle. Although the choice of parameters above was adopted, it has been noted that variations in the values of both α and κ_ω of up to 50% produced a little effect on the overall performance of the segmentation.

The resulting 12 images are the multi-channel feature set, they are used for the formation of a $12 \times (M \times N)$ feature matrix, where $[M, N]$ are equal to the input image dimensions, with each column representing a feature vector.

The statistical and multi-channel features are then combined to form a set of $12 + 15 = 27$ texture stacked images.

3.6 Number of Clusters

Depending on how descriptive the input features are of the underlying data, they contain inherent clusters corresponding to the different categories, ideally each cluster is compact and isolated from clusters corresponding to other categories. Clustering algorithms identify densely populated regions in feature space and assign class membership labels to each data point. The success of a classifier is directly related to the degree of clustering and the separation between clusters.

In order to segment the image into regions representing different clusters with different visual texture, it is important to be able to determine automatically (without a priori knowledge) the number of clusters depicting each image partition. Estimating the true number of clusters in multivariate data is one of

the most venerable problems in cluster analysis, and several indices have been proposed to provide such an estimate [67, 68]. An internal index of partition adequacy compares the given proximity matrix with the partition of the objects obtained from a cluster analysis without reference to category labels or other external information.

The modified Hubert (MH) index proposed by Dubes [67, 69] has proven to perform significantly better than other such indices, and with higher reliability. This index was thus adopted to determine the number of clusters in the borehole data. Adapted from the Hubert gamma statistic [70, 71], this index is the point serial correlation coefficient between the matrix of inter-pattern distances and the distances recovered from the clustering solution.

A clustering solution is a partition $\{C_1, C_2, \ldots, C_k\}$ of the integers from 1 to m such that $i \in C_k$ if in_i is in the kth cluster. The centre of C_k is denoted by the $d - place$ vector:

$$\mathbf{m}_k = \frac{1}{m_k} \sum_{i \in C_k} in_i \tag{3.29}$$

where m_k is the cardinality of C_k and

$$m = \sum_{k=1}^{d} m_k \tag{3.30}$$

The Euclidean distance $d - place$ vectors in and y is defined as:

$$\|in - y\| = \sqrt{(in - y)^T (in - y)} \tag{3.31}$$

where T denote matrix transpose. Let L be the label function that maps the set of patterns to the set of cluster labels such that:

$$L(i) = k \qquad if \quad i \in C_k \qquad (3.32)$$

with $M = m(m-1)/2$,

$$r = \frac{1}{M} \sum_{i=1}^{m-1} \sum_{j=i+1}^{m} \|in_i - in_j\| \cdot \|m_{L(i)} - m_{L(j)}\| \qquad (3.33)$$

$$M_p = \frac{1}{M} \sum_{i=1}^{m-1} \sum_{j=i+1}^{m} \|in_i - in_j\| \qquad (3.34)$$

$$M_c = \frac{1}{M} \sum_{i=1}^{m-1} \sum_{j=i+1}^{m} \|m_{L(i)} - m_{L(j)}\| \qquad (3.35)$$

$$\sigma_p^2 = \frac{1}{M} \sum_{i=1}^{m-1} \sum_{j=i+1}^{m} \|in_i - in_j\|^2 - M_p^2 \qquad (3.36)$$

$$\sigma_c^2 = \frac{1}{M} \sum_{i=1}^{m-1} \sum_{j=i+1}^{m} \|m_{L(i)} - m_{L(j)}\|^2 - M_c^2 \qquad (3.37)$$

The MH measure for clustering $\{C_1, C_2, \ldots, C_k\}$ is:

$$MH(k) = \frac{r - M_P M_c}{\sigma_p \sigma_c} \qquad (3.38)$$

As observed by Dubes [67], when the data contains a strong clustering, the MH index statistic increases monotonically as the number of clusters increases, and then levels off with "significant knee" formed at the true number of clusters. The index will be 1 for the trivial clustering in which each pattern is an individual cluster, and is not defined for a one-cluster clustering. A decision rule is thus adopted that searches for this significant knee in the curve of $MH(k)$ as k varies

from 2 to k_{max}, where k_{max} is the maximum estimated number of clusters in the data.

Suppose the true number of cluster is k_{true}. The clusterings with $k > k_{true}$ will be formed by breaking the true clusters into smaller ones, and as a result the correlation between $\|in_i - in_j\|$ and $\|m_{L(i)} - m_{L(j)}\|$ matrices will be high. The clusterings with $k < k_{true}$ clusters, however will be formed by merging the true clusters, hence reducing the correlation. Therefore, assuming that the texture features provide strong discrimination between different texture categories, a significant knee should be observed in the plot of MH(k) at the true value of k.

The knee function at k clusters, $S(k)$ is the tangent of the acute angle between the lines defined by $MH(k+2)$, $MH(k+1)$ and $MH(k)$. The larger this tangent, the more significant the knee at k clusters. Although the first significant knee can be detected by setting a threshold of significance, it may also be sought by eye. Figure 3.6 demonstrates this knee at four categories for the borehole visual texture features.

3.7 Representative Categories for Image Data

As discussed in Section 3.6, and Figure 3.6 shows image data (Figure 3.7) contains four different textures or visual properties. Hence in all subsequent analysis and investigation, the data is considered to consist of four categories of texture.

Typical patches that represent four categories are selected to perform quantitative analysis of borehole data. Patches of (32×32) pixels were selected manually from borehole image (e.g Figure 3.7), and compiled together in the form of a (256×256) mosaic image as shown in Figure 3.8. The four quadrants of the
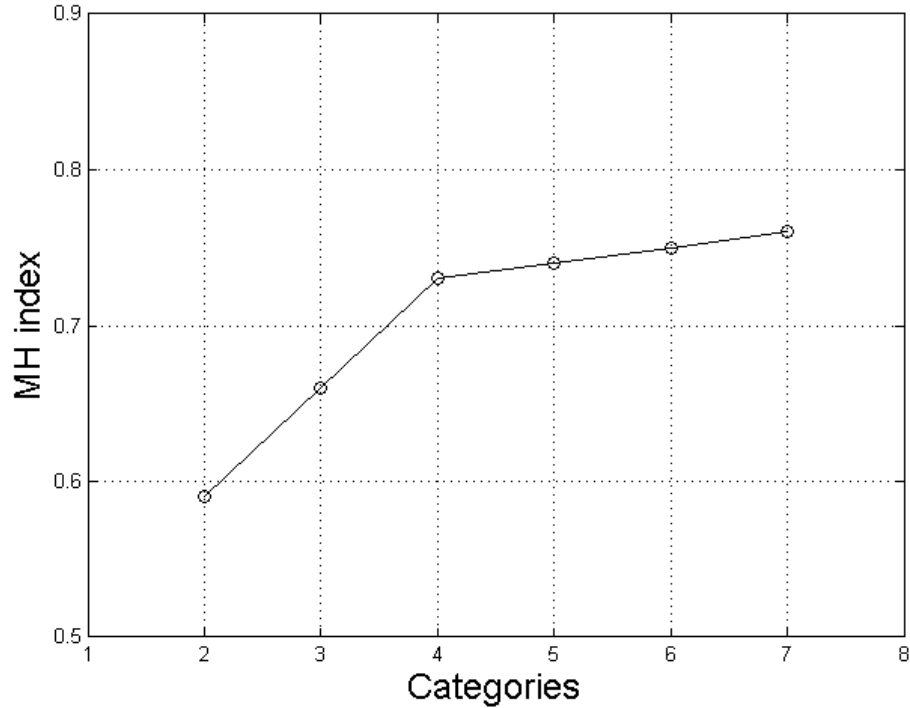
Figure 3.6: Plot of MH index versus number of categories showing significant knee at four classes in Figure 2.2

composite image which correspond to the four selected image categories will be used for classifier training and for performance estimation.

3.8 Competitive Learning

In competitive learning, an input vectors is classified into one of K categories based on detected cluster in training set in. The network weights are organised during rejected dissimilar vectors, and the most similar or called winner is activated for weight building. When the network is trained correctly, all cluster members in_i will have the same winner. *Kohonen network* is called on the network to be trained and as shown in Figure 3.9.

The process of dividing the input space into a number of adjacent subspaces or clusters and presenting each input in_i by the label of cluster is called *vector*
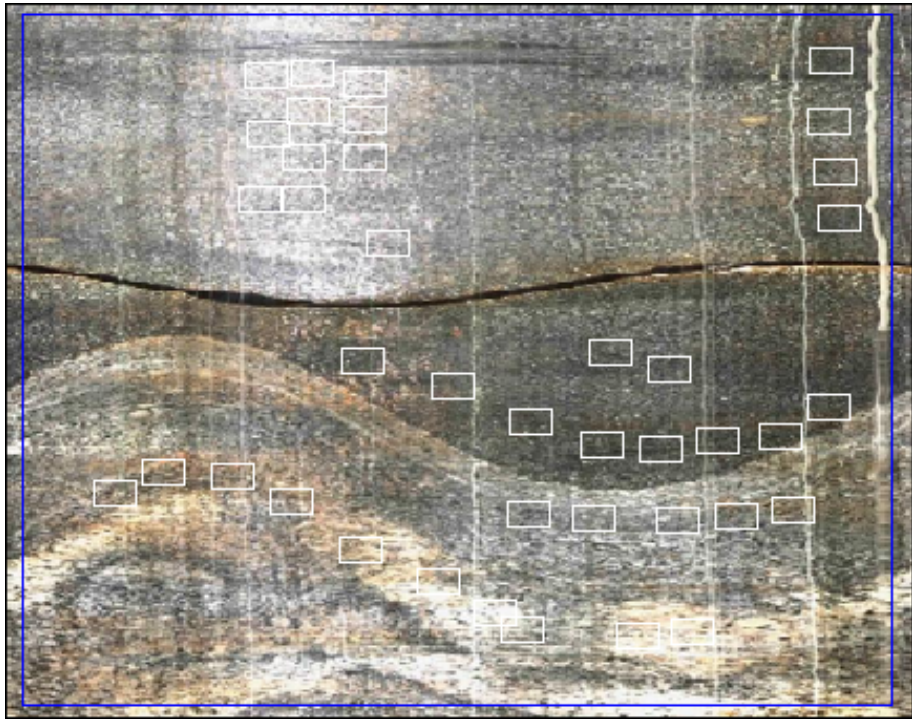
Figure 3.7: Patches selected from borehole image, representative of different visual textures
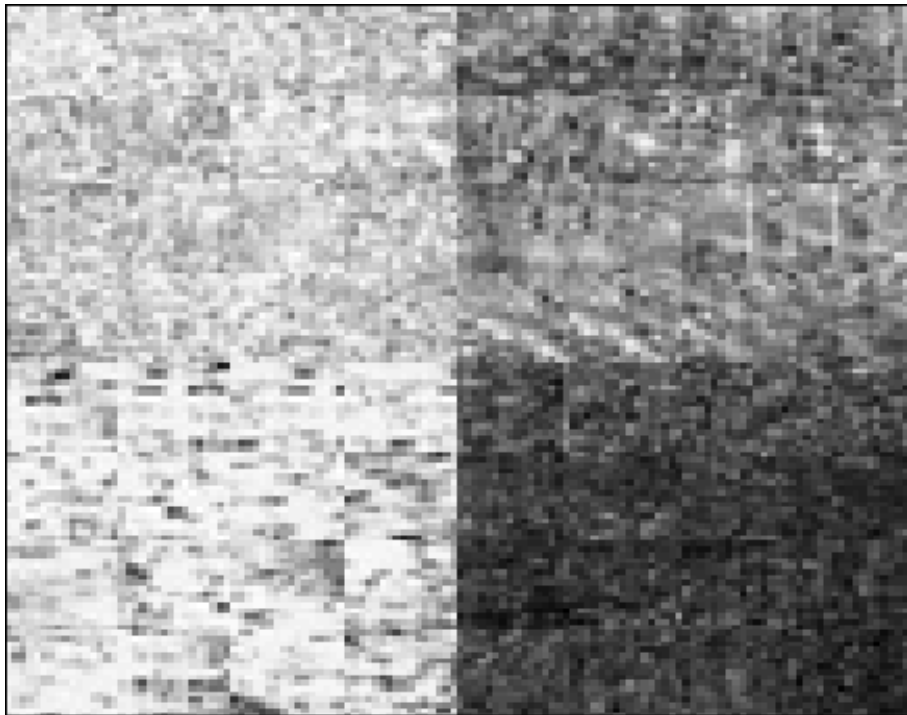

Figure 3.8: Four-quadrants image of representative categories
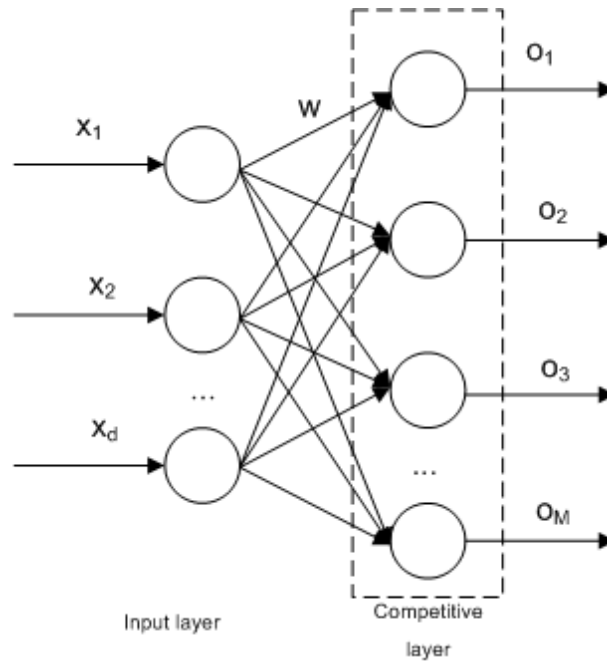
Figure 3.9: Simple Kohonen competitive learning network [6]

quantisation. In other words, the input vectors in of dimension m are transformed or mapped to one of a finite number of classes of k dimension , where each class is represented by prototype vector $w_i(i = 1, 2, \ldots, k)$. The index i of dimension $k < m$ becomes the class label of in. Vector quantisation mapping is a nearest neighbour mapping defined by Euclidean distance.

Unsupervised learning implies the absence of a teacher and no knowledge beforehand of what the output should be for any given input. The network acts as a regularity detector and tries to discover structure in the patterns presented, based on global competition between neurons. Although unsupervised classifiers do not require *a prior* class membership information, most neural network classifiers require, the number of categories to be known. While in many cases this is obvious or easily obtained, in order to deliver a fully-automated unsupervised classifier the number of clusters must be estimated by the classifier from the data itself.

Self-organisation or unsupervised learning process is when the network can learn a weight vector without any explicit clue of the existence of the cluster in the input. The processing of input *in* from the training set follows the expression:

$$out = \Gamma(W \times in) \tag{3.39}$$

where:

$$W = (w_1 \ w_2 \ \ldots w_k) = \begin{pmatrix} \mathbf{w}_{11} & \mathbf{w}_{12} & \ldots & \mathbf{w}_{1k} \\ \mathbf{w}_{21} & \mathbf{w}_{22} & \ldots & \mathbf{w}_{2k} \\ \vdots & \vdots & \ddots & \vdots \\ \mathbf{w}_{m1} & \mathbf{w}_{m2} & \ldots & \mathbf{w}_{mk} \end{pmatrix}$$

is the weight matrix and the diagonal elements Γ being continuous activation functions operating component-wise on entries of the vector Win a feedforward manner. Before the learning process is started, all weight are initialised to small random values and normalised to unite circle.

$$\hat{w}_i = \frac{w_i}{\|w_i\|} \tag{3.41}$$

where $\hat{w}_i$ is normalised weight vector.

Each input pattern is presented one at a time and the output units compete to represent the input pattern. Based on Euclidean distance metric, the winning neuron is the one which is the closest to the current input pattern in, such that:

$$\|in - \hat{w}_c\| = min_{i=1,2,\ldots,m} \{\|in - \hat{w}_i\|\} \tag{3.42}$$

where c denotes to the winning neuron. Competitive learning is also know by *winner-take-all* learning. Leaning process is performed only by the winning neu-
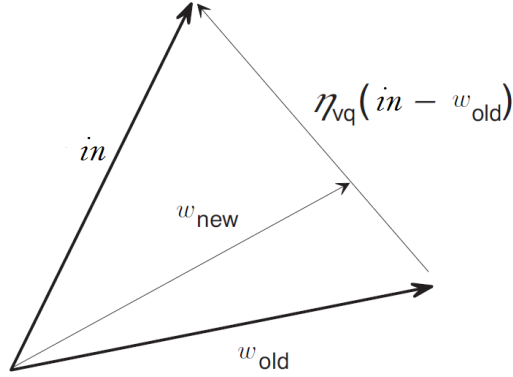
Figure 3.10: Illustration of winner-take-all weight update [6]

ron and its weight

$$
\hat{w}_i(t+1) = \begin{cases} \hat{w}_i(t) + \eta_{vq}(in - \hat{w}_i(t)) & for\ the\ winner\ i = c \\ \hat{w}_i(t) & for\ i\ \neq c \end{cases} \tag{3.43}
$$

where η_{vq} is a suitable positive learning constant that may be fixed or decreased as learning progresses. The weight vectors are rotated towards the centres of gravity of the input clusters as illustrated in Figure 3.10.

After a predefined number of training epochs, the training stage stops, and each $\hat{w}_i$ presents the centroid of an ith decision region and the result is partitioning the pattern space into non-overlap region or clusters. The cluster formation process is described in detail in [72, 73] and [74], and is equivalent in effect to the traditional k-means clustering technique.

3.9   Image Segmentation

It specifies how the rule of classification are constructed and how the data is used. The separation of classes in the feature space determines the success of the classifier. Generally, the feature space is multi-dimensional and it might have
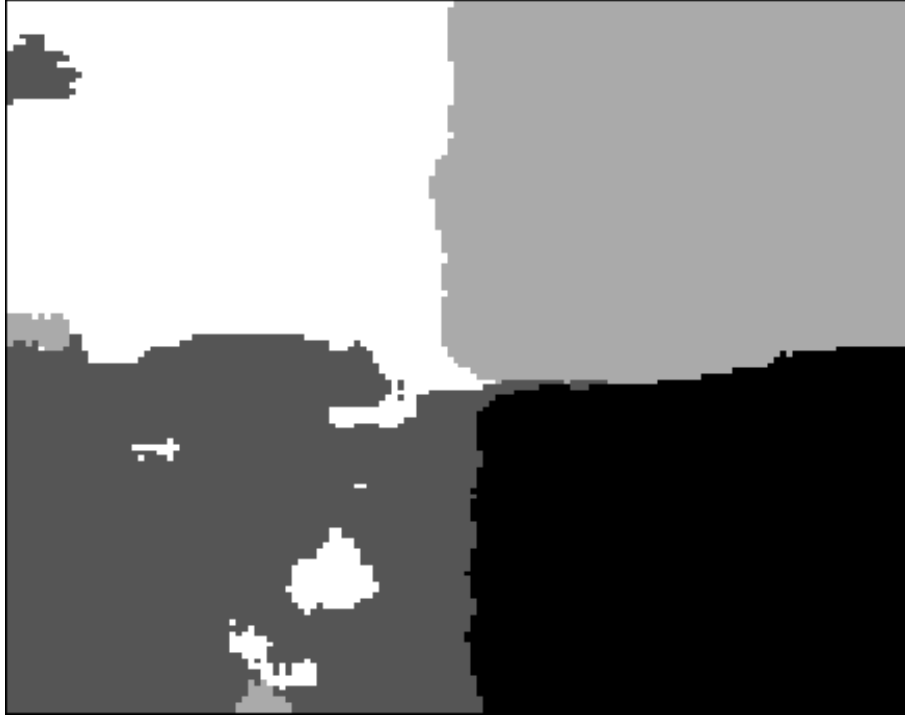
Figure 3.11: Results of four-quadrant image in Figure 3.8

overlapped classes. If the class probability density functions is known, the best classifier option is Bayesian that maximises correct classification by associating regions of input space with the class with the largest probability density. However, in real experiment, class probability density functions are unknown so the choice here is neural network classifiers [75]. Neural network classifier is easy to implement and modified in MATLAB .

In particular, the random cross-validation hold-out sample used for training is 10% of the total size of the feature set, and the remaining 90% is used during recall. During training, the number of input neurons is matched to the number of features in the feature vector, and the number of output neurons set to 4, the number of detected texture categories. At the end of the clustering process, image are partitioned into four different regions as shown in Figure 3.11 and Figure 3.12.
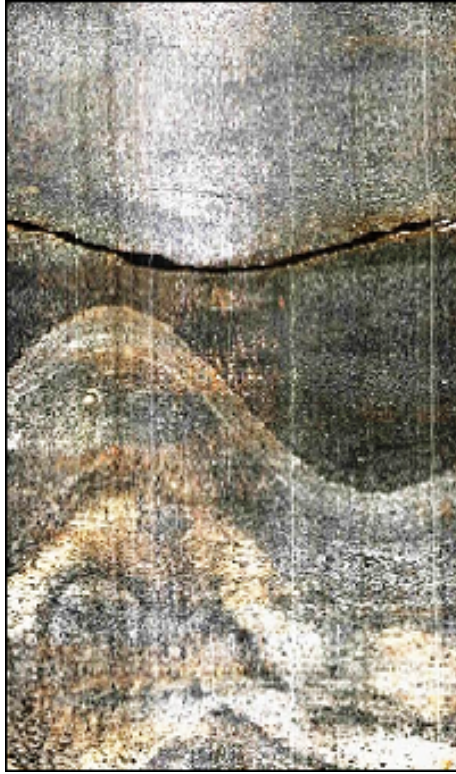
(a)
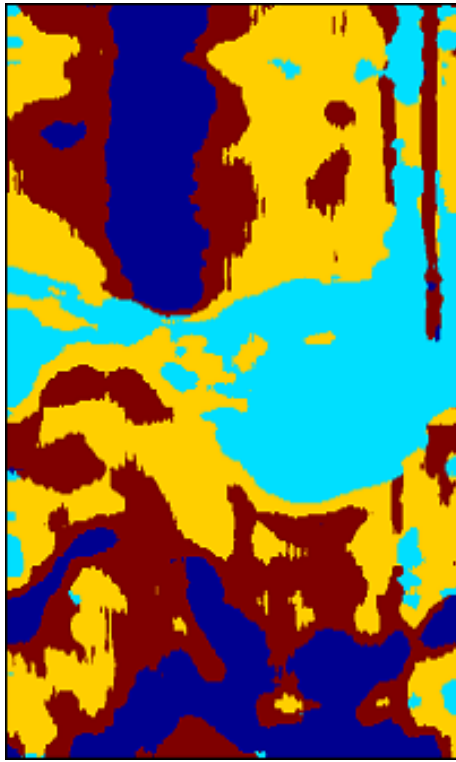
(b)

Figure 3.12: (a) Multiple layers of volcanic rock not exhibiting visible fractures, (b) Image segmentation result

3.10 Clustering Performance Measurement

The performance of a classifier is measured according to its ability to label unseen data correctly. Before this data is made available, only an estimate of the true performance can be made using the classification of the data. This is given either in the form of an error rate or classification rate, computed from the number of misclassified samples and the size of the test set. The generalisation error is estimated using the cross-validation method. The model is developed using the cases in the learning set and its predictive accuracy assessed using cases in the test set. The hold-out estimate is repeated for different portions of the data and the results averaged for a stable and unbiased estimate of the generalisation error. The resulting rate represents the percentage of cases that the trained classifier is expected to classify correctly, subject to the assumption that all examples are independent and sufficiently representative of the data to be encountered in practice.

As apparent in Figure 3.12(a), different regions of the image exhibit different visual properties and contain four categories of texture verified by the MH index and represent the number of clusters. Typical patches of these four categories can be seen in Figure 3.8, combined together in the form of a four-quadrant image that is used to calculate the classifier error rate. Pixels in the four-quadrants image are clustered into four groups.

Figure 3.13 shows the segmentation results for the four-quadrant image of representative categories, segmented unsupervised using both the 15 statistical texture descriptors listed on page in Section 3.4 (Figure 3.13(a)), and the combined 27 features (Figure fig:patch-class). The correct classification rates for the two cases are respectively 82.9% and 93.6%, indicating clearly that compared to

the statistical texture features, the combined features produce clusters that are more compact than statistical texture features, which lend themselves better to unsupervised cluster analysis.

3.11   Summary

This chapter has presented a texture-based segmentation method for borehole data segmentation. The concept of visual texture is introduced as the key visual cue for identification and recognition of homogeneous regions. Specifically, statistical textures and multi-resolution textures segmentation and the feature extraction methods are discussed in details. The feature extraction procedure, the process of neural network pattern classification and image segmentation are described in this chapter as well.

The sequence of processing stages that transform a borehole images into a segmented image representing different categories of texture is presented. Thus, a general framework for the automated and unsupervised segmentation of borehole images is developed, with the particular objective of locating a planar fractures and layers. The result of the processing is a segmented image with clearly separated regions, which makes unclear fractures and layer edges to be extracted using Canny edge detection in next processing step.
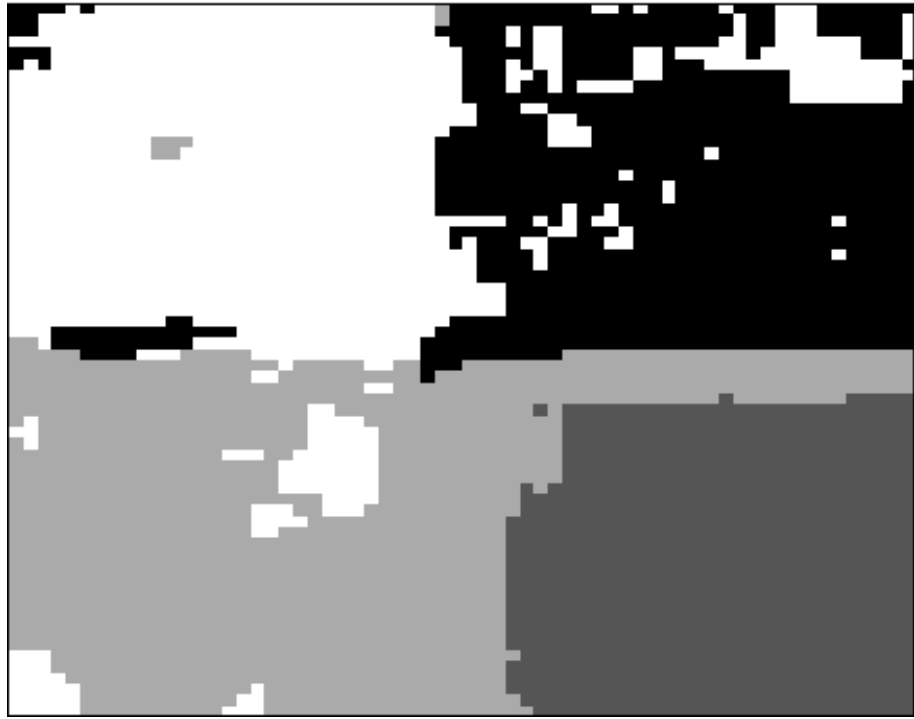
(a)
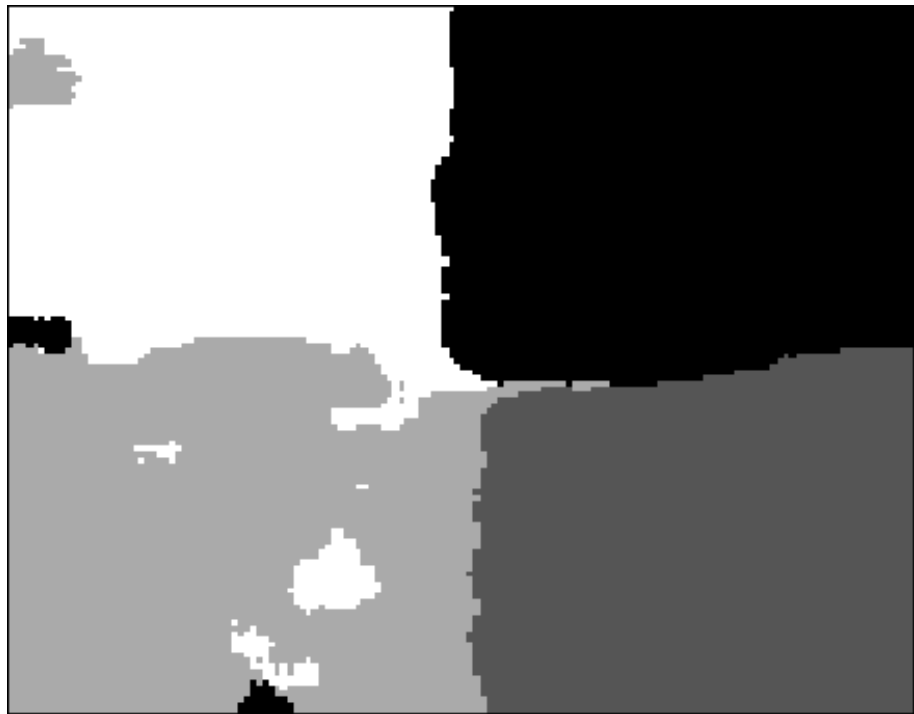
(b)

Figure 3.13: (a) Unsupervised classification of 15 statistical features (b) Unsupervised classification of combined features

Chapter 4

Edge Detection and Fracture Characterisation

4.1 Introduction

In the previous chapter, the borehole data are segmented into different regions based on visual texture. The first step in characterising shapes in an image is to detect the outline of all shapes present. This outline detection problem is a common image processing task of edge detection, and several techniques are available in the image processing literature. Classical edge detectors have no smoothing filter, and they are only based on a discrete differential operator. The earliest popular works in this category include the algorithms developed by Sobel (1970), Prewitt (1970), Kirsch (1971), Robinson (1977), and Frei-Chen (1977) [76]. They compute an estimate of gradient for the pixels, and look for local maxima to localise step edges. They often estimate the gradient magnitude of an image $f(x, y)$ at point (x, y) by:

$$g_{x,y} = \nabla f = |\nabla f| = \sqrt{g_x^2 + g_y^2} \qquad (4.1)$$

where g_x and g_y correspond to the partial derivatives $\frac{\delta f}{\delta x}$ and $\frac{\delta f}{\delta y}$ respectively.

Typically, the mentioned edge detection methods are simple in computation and capable to detect the edges and their orientation, but due to lack of smoothing stage, they are very sensitive to noise and inaccurate. The proposed method approach develops various processing tools to refine and automate the edge detection process to the greatest extent possible. It involves modified Canny edge detection and skeletonisation. The goal is to detect the abrupt changes in intensity associated with the envelope edges of fractures.

4.2　Canny Edge Detection

Canny [77,78] proposed a method that was widely considered to be the standard edge detection algorithm in the industry, and still it outperforms many of recent algorithms [79]. In regard to regularisation explained in image smoothing, Canny saw the edge detection as an optimization problem. He considered three criteria desired for any edge detector: good detection, good localisation, and only one response to a single edge. Then, he developed the optimal filter by maximising the product of two expressions corresponding to two former criteria (i.e. good detection and localisation) while keeping the expression corresponding to uniqueness of the response constant and equal to a pre-defined value. The solution (i.e. optimal filter) was a rather complex exponential function, which by variations it could be well approximated by first derivative of the Gaussian function. This implies the Gaussian function as the smoothing operator followed by the first derivative operator. Canny showed that for a 1-D step edge the derived optimal filter can be approximated by the first derivative of a Gaussian function with variance σ as follow:

$$f_\sigma(x) = \frac{dG_\sigma(x)}{dx} = -k\frac{x}{\sigma^2}\exp(-\frac{x^2}{\sigma^2}) \qquad (4.2)$$

To solve an image affected by noise, Canny proposed the use of two filters representing derivatives along the horizontal and vertical directions as follow:

$$f_\sigma(x,y) = [f_\sigma(x) * G_\sigma(y) \quad G_\sigma(x) * f_\sigma(y)] \qquad (4.3)$$

As the segmented image shows clearly the separated regions as apparent in Figure 4.1(a), there are a number of approaches to the boundary-detection problem in image processing. The method adopted here makes use of a modified Canny edge detector. The steps of the modified Canny edge detector are as follows:

1. Spurious noise is removed by convolving the image with a Gaussian function.

2. The intensity gradient at each pixel in the convolved image is computed using a directional operator.

3. Since fractures are found to be more horizontal than vertical [22], an edge point is defined to be a point whose gradient is locally maximum in the vertical direction of the gradient.

4. Non-maximum suppression is performed to track all pixels that are identified as strong edge points and sets to zero all pixels that are not actually edge points.

5. To eliminate streaking, hysteresis is then carried out by using two thresholds T_1 and T_2, with $T_1 < T_2$, T_1 and T_2 thresholds are initialised by random values. Pixels are then classified into either *strong* or *weak* based on their value. The edge pixels with values greater than T_2 are said to be *strong*,

and edge pixels with values between T_1 and T_2 are said to be *weak* edge pixels.

6. The algorithm performs edge linking by incorporating the weak pixels that are connected to the strong pixels.

An advantage of applying this to the segmented image is that it does not need to manually tune any parameters (low and high threshold values (T_1, T_2) and the standard deviation of the Gaussian filter σ) as the regions are clearly separated, which reduces the manual editing required. However, smoothing stage of Canny edge detection affects on some segmented regions (as shown in Figure 4.1(b)).

4.3 Edge Thinning

A skeletonisation algorithm was developed specifically for the task of increasing the resolution of the above result by reducing extended blocks of pixels into one pixel-thick segments. This is achieved by passing through the image twice, once in the horizontal direction and once in the vertical direction. In the horizontal pass, a horizontal 5×1 mask is scanned across the whole image, and whenever the pixel intensity combination [01110] is encountered, it is replaced by the mask [00100]. Similarly, in the vertical pass, all occurrences of the intensity combination $[01110]^T$ are replaced by $[00100]^T$. This skeletonisation algorithm has proven to be very successful when applied to detected edge images as shown in Figure 4.2. The skeletonisation process reduces the computational time of Hough transform peak selection and fracture characterisation by 15%.
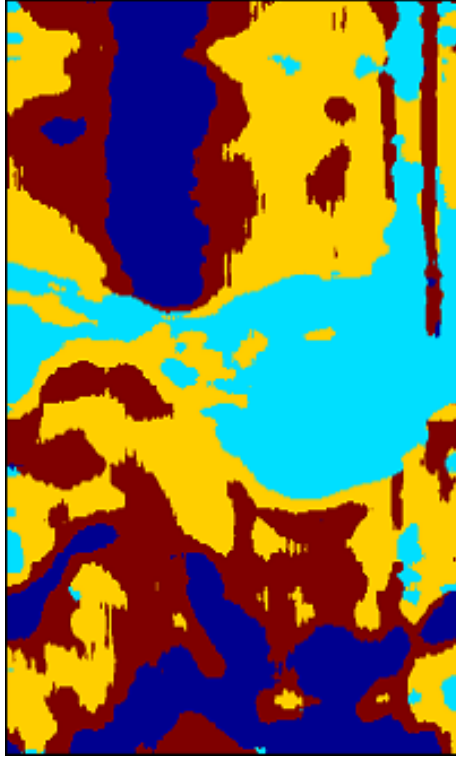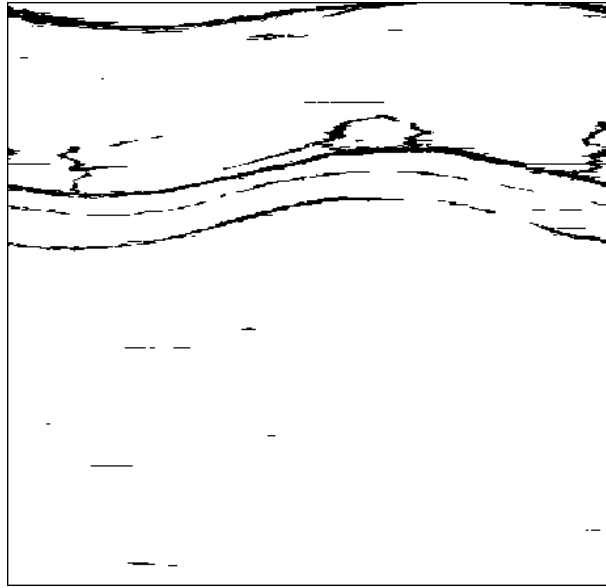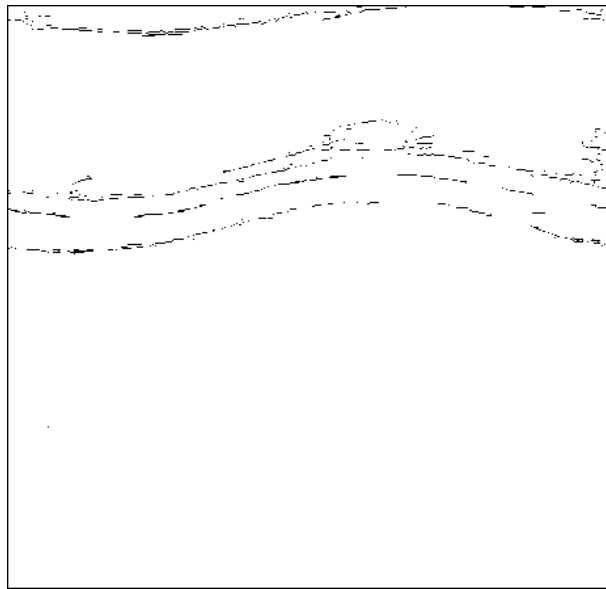
(a)

(b)

Figure 4.1: (a) Segmented image (b) Edge detection result using modified Canny edge detection

(a)

(b)

Figure 4.2: (a) Detected edge, (b) Edges after custom skeletonisation

4.4 Pattern Recognition

4.4.1 Hough Transform and Parameter Estimation

Since the boundaries are determined in the edge detection stage, the exact shape of the edge segments that correspond to fractures are found using pattern recognition in order to characterise these curves fully. The Hough transform is an established method for detecting complex patterns of points in binary image data, and has been known to perform well in presence of noise, extraneous data and occlusions. This is achieved by determining value of parameters which characterise these patterns. Spatially extended pattern are transformed so that they produce spatially compact features in parameters space, converting a difficult global detection problem in image space into a more easily solved local peak detection problem in parameter space [80, 81].

Successful application of the Hough transform requires a definite knowledge of the type of curves sought in order to obtain analytic relationships between image and transformation-space parameters. As described in Section 1.2, fracture appear as sinusoid if the borehole is cylindrical and are cutting by a planar fracture (as shown in Figure 1.3). Mathematically, fracture is expressed as follows:

$$y = A\sin(\omega x + \theta) + y_0 \tag{4.4}$$

where A is the amplitude, y_0 is baseline position, θ is the phase and ω is the angular frequency ($\omega = 2\pi/T$) and T is the image width (or borehole circumference). In borehole televiewer images, ω can be considered constant, and the sinusoidal waves can therefore be characterised completely by specifying A, θ and y_0. The Hough transform can therefore be interpreted as a one-to-many mapping from a binary image point (x, y) to a set of possible parameter values (A, θ, y_0). This

corresponds to calculating the parameters of all sinusoidal waves which belong to the set which pass through any given image point as.

To increase the computational efficiency and to facilitate interpretation of the results, the HT is performed in two dimensions (A, θ) with the value of the third offset parameter y_0 found using a coarse-to-fine search strategy. By taking 10% of A_{max} (where $A_{max} = r\tan(\beta)$, β is the maximum expected fracture dip angle and r is the borehole radius, scaled to pixels) as a search length in the coarse search to find the closest location for the actual offset value, the fine search finds the actual offset value. Each point in the binary edge image is transformed into an inverse-sinusoid $(\sin^{-1})$ in (A, θ) parameter space using:

$$A = \frac{y - y_0}{\sin(\omega x + \theta)} \tag{4.5}$$

where $0 \leq A < A_{max}$, and $0 \leq \theta < 2\pi$.

The parameter space is subdivided into discrete accumulator cells, and the points (A, θ) rounded to the nearest accumulator bin. For each value of (x, y), these discrete inverse-sinusoid are superimposed over each other in the accumulator which functions as a two-dimensional histogram. The magnitude of the accumulator surface at any point indicates the likelihood of a sinusoid in the image having parameters A and θ corresponding to the co-ordinates of that point as shown in Figure 4.3.

The accuracy of the information extracted from the Hough transform depends on the manner in which the accumulator is interpreted. Although selecting the peaks of the accumulator surface succeeds in locating most targets to a considerable degree of accuracy, in situations with a more complex and noisy image and
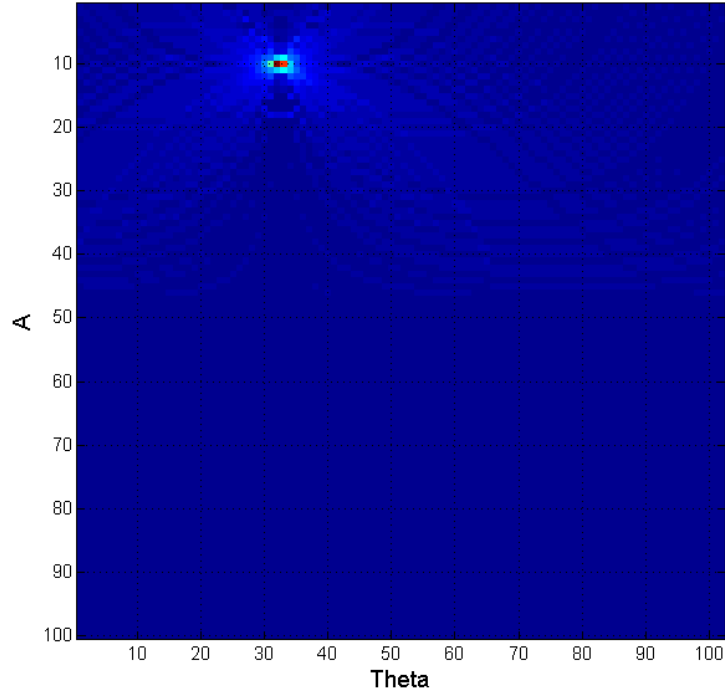
Figure 4.3: Hough transform accumulator

the edges are hard to be found by using global thresholding, this direct approach was found to occasionally generate misleading results. In addition to the magnitude, for each peak detected, two other attributes are computed to eliminate false peak detection. Based on x value of each image point, *Maximum pixel chain*, that represents the maximum number of connected pixels along a sinusoid, and *Maximum horizontal gap*, that represents the maximum distance between two adjacent sinusoid segments are calculated. This give a strong indication of how long the candidate edge is spreading over the image and for any false sinusoids that are detected due to the noise or intersection fractures. Empirical threshold values for maximum chain and maximum gap are then used to filter the peak selection process prior to sinewave synthesis.

The dip direction with a cylindrical borehole is given by the phase of the sinusoid minimum, while the dip angle gives the steepest angle of descent of a tilted bed or feature relative to a horizontal plane ($dip\ angle = \arctan(\hat{A}/r)$,

where $\hat{A}$ is the (scaled) sinusoid amplitude (in meters) and r is the borehole radius [18]).

4.5 Detection Results

The developed detection method explained in previous chapters that is based on the use of visual texture segmentation, neural network, modified Canny edge detection and modified Hough transform has proven to be rapid, accurate and robust. The data set used in the tests and the results are shown in Appendix A. Using a PC with Intel Core i3 running at 3.4 GHz processor running MATLAB R2013a, the detection result has been achieved in a matter of seconds (between 30 and 120 s) depending on the length of the borehole data image. The output is readily understood by people not routinely involved with fracture interpretation as each fracture is outlined with synthetic sinusoid.

The proposed method was implemented using MATLAB and applied to several optical, acoustic and resistivity borehole images and proven to be proficient even at locating partial features, as marked in red in optical data as shown in Figures 4.4, 4.5 and 4.6, and marked in green for acoustic data and resistivity as shown in Figures 4.7 and 4.8 respectively. It was found (and verified by expert geophysicist interpretation) that this automatic annotation correctly labels all the rock features, including layers and cross-cutting partial fractures, with a 1% false positive rate overall.

Another significant achievement of the proposed method is the increasing picking accuracy of planar discontinues located between textures that varies from low to high pixels intensity contrast as shown in Figure 4.4(b), these fractures would not have been detected using only edge detection but using the visual texture

enabled the fractures to be detected. In addition, Figure 4.5(b) shows that the proposed method has the ability to detect accurately cross-cutting fractures and phase-shift between the detected fractures due to fault displacements. Low contrast, steep fractures are also detected, as shown in Figure 4.6(b).

In addition, using Canny edge detector to extract edges from segmented image does not need any parameter tuning by the operator. Moreover, the proposed method is using 2-D instead of 3-D Hough transform to find the parameters, which reduces computational time and memory requirement. In addition, the two attributes i.e. *Maximum pixel chain* and *Maximum horizontal gap* with the accumulator magnitude to eliminate any false sinusoids that are detected due to the noise or intersection fractures.

An intuitive GUI tool was built (as described in Appendix C), offering many capabilities to the operator. The built GUI tool provides an output that is more readily understood by people not routinely involved in borehole data interpretation, and shows very good performance and user-friendliness.

4.6 Summary

This chapter has presented the edge detection and mapping techniques developed and employed. These stages have been integrated in such a way that the each subsequent layer introduces refinements to the results of the previous layer, progressively reducing the redundancy in the image information. The system requires a number of arbitrary constants to be set, such as the threshold levels and the window sizes, and empirical values have been selected which have been found to work successfully with the range of borehole data investigated.
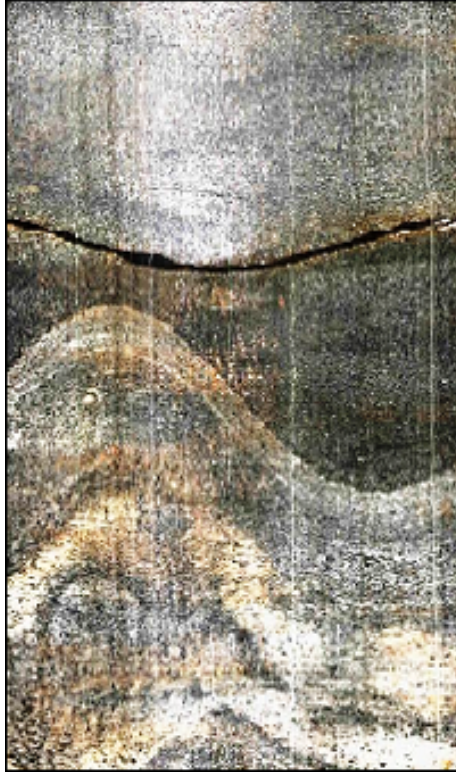
(a)

(b)

Figure 4.4: (a) Multiple layers of volcanic rock not exhibiting visible fractures,
(b) Poorly-defined rock layers correctly delineated

(a)
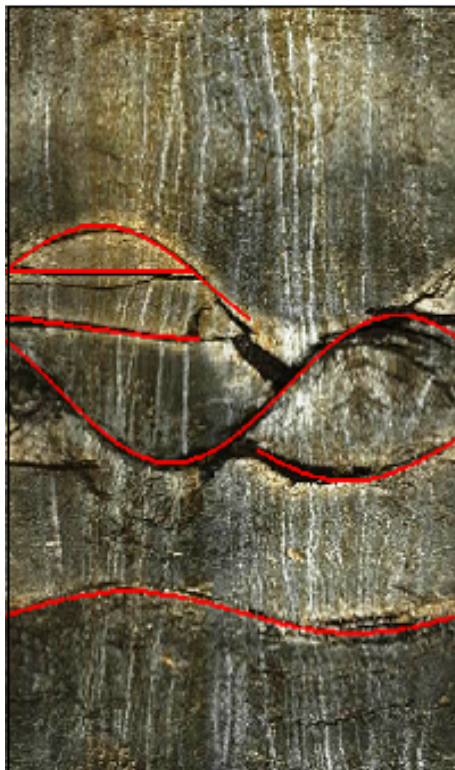
(b)

Figure 4.5: (a) Cross-cutting and partial fractures Optical, (b) Cross-cutting and partial fractures detected automatically

(a)

(b)

Figure 4.6: (a) High angle fracture, (b) High angle and disjointed fractures characterised

(a)

(b)

Figure 4.7: (a) Acoustic borehole image- Amplitude data, (b) Detection result

(a)

(b)

Figure 4.8: (a) Resistivity borehole image (b) Detection result

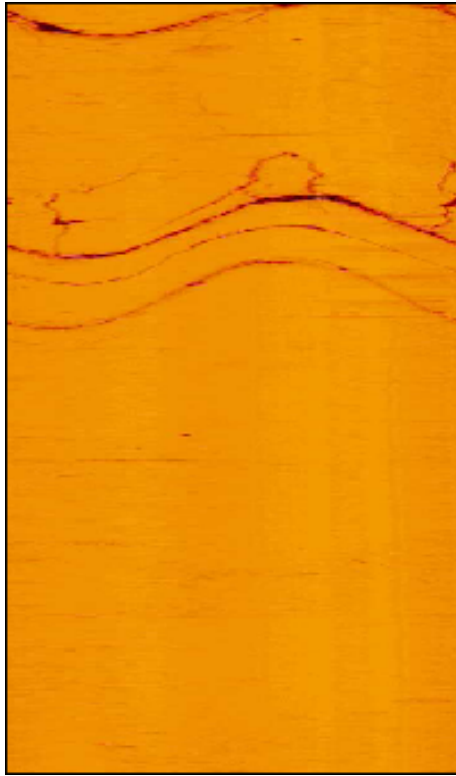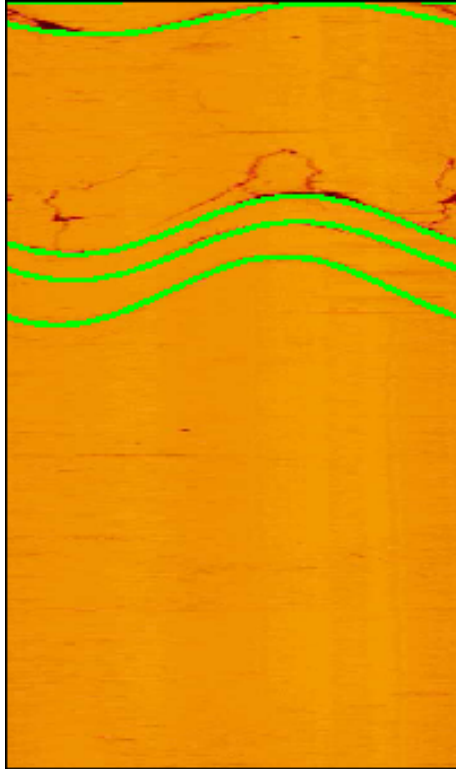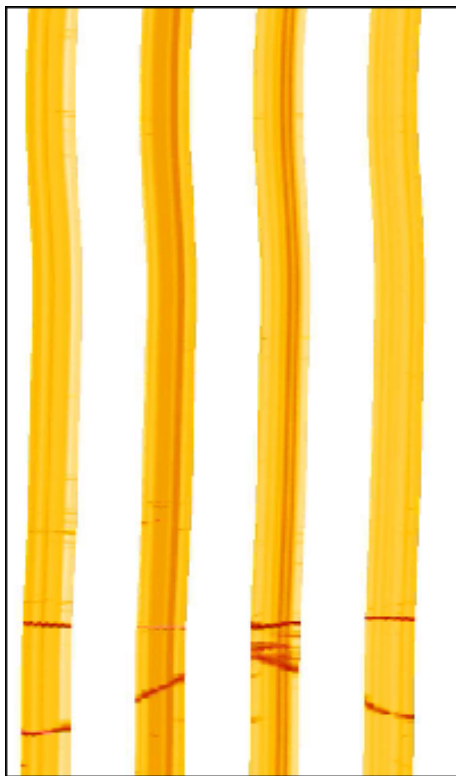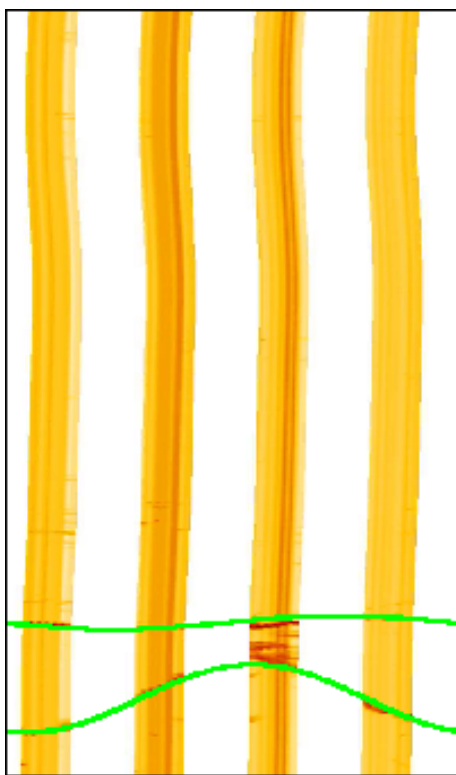The obtained results show that this method has great potential in automating the process of borehole image annotation and interpretation. In addition, using Canny edge detector to extract edges from segmented image does not need any parameter tuning by the operator. Moreover, the proposed method is using 2-D instead of 3-D Hough transform to find the parameters, which reduces computational time and memory requirement. In addition, the two attributes i.e. *maximum pixel chain* and *maximum horizontal gap* with the accumulator magnitude eliminate false sinusoids that are detected due to the noise or intersection fractures. Moreover, this chapter has shown the results after testing the proposed algorithms and methods to automatically detect and characterise borehole fractures. All algorithms were implemented using MATLAB as functions, and in order to facilitate the execution of these functions. The developed algorithms have been verified against variety types of borehole data set, fractures have been successfully detected and characterised.

The results obtained so far after using these methods have been extremely promising in terms of of the ability to detect non-distinct layers and fractures, cross-cutting and partial fractures, and high angle and disjointed fractures. This would make the proposed techniques suitable in situations requiring automatic (or semi-automatic) near real-time processing and interpretation of large volumes of borehole data, hence, greatly reducing time, human interference and experimental errors.

Chapter 5

Borehole Modelling and Multi-sensor Borehole Data

This chapter presents borehole shape modelling and distorted fracture detection and characterisation in deformed borehole geometry, In addition, multi-sensor borehole data (optical and acoustic) combining in order to enhance fracture detection accuracy.

5.1 Borehole Modelling

Fractures, which are used to investigate the underground from geophysical point of view, are the key factor to understand the stress situation around borehole wall. It appears as sinusoids if assume the borehole to be in-gauge hole (cylindrical) and are cutting by a planar fracture, as a result the unwrapping image will show an ideal sinusoid as shown in Figure 5.1. Practically, if the borehole images are properly acquired from a uniform cylindrical drilled borehole and processed, they can help to identify the followings:

(a) Fractures, layers and veins

(b) Intrusions for mining

76
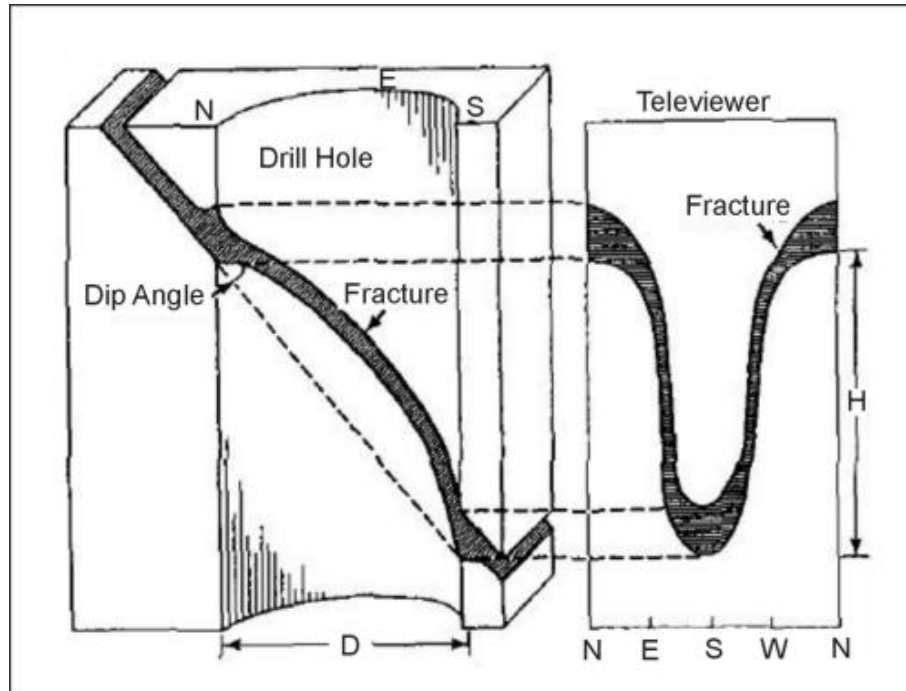
Figure 5.1: Three-dimensional view of a fracture and appearance of the same fracture on an acoustic televiewer log. D is borehole diameter and h is the length of the fracture intercept in the borehole [7]

(c) Geotechnical assessments

There are four common borehole geometries as shown in Figure 5.2:

(a) An in-gauge hole that has dimensions of the drill bit.

(b) A breakout has one diameter elongated but the orthogonal diameter remains at the original bit size.

(c) A key seat occurs when the drill-string wear has caused a pear-shaped borehole. The risk for key seats, or drill-pipe wear, increases with increasing borehole inclination (as well as lengths).

(d) A washout appears as an increase in all dimensions of the borehole.

Fracture shape is directly related to the actual borehole geometry which based on breakout theory. Breakout theory was originally proposed by Bell [10] and Gough [7], based on the equations of Kirsch [11]. The borehole breakout method

Figure 5.2: Examples of common borehole geometries and their expression [8]

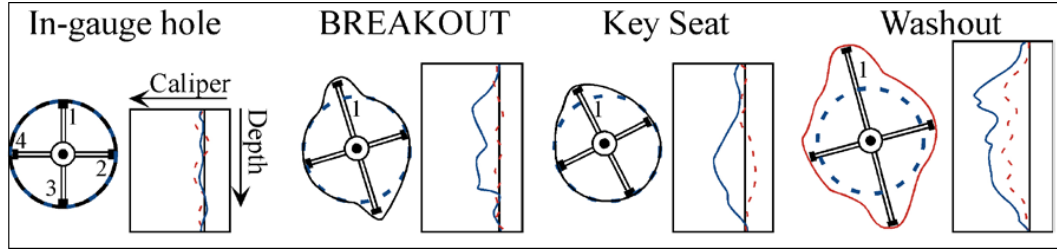is an important indicator of horizontal stress orientation, particularly in a seismic regions and at small and intermediate depths.

In an ideal case, when the borehole is in-gauge (circular), a planar fracture appears as an ideal sinusoid. However, when the borehole wall is elongated or compressed, the fracture appears as a distorted sinusoid. From this, the dip and dip angel are extracted, which give curial information about the geometry of the fracture.

To overcome the limitations of existing methods to detect distorted fracture signature, a new method based on non-linear least squares ellipse fitting and a modified version of Hough transform has been proposed. The new method identifies the actual borehole geometry, detects and characterises the distorted fracture in an arbitrary-shaped borehole.

5.1.1 Borehole Shape Modelling

Acoustic borehole data are used to for borehole shape modelling. Acoustic tool collects two types of detailed acoustic data (travel time and amplitude images as shown in Figure 2.3) of the borehole wall that provides information on the borehole diameter and acoustic impedance. Detailed information about the borehole shape can be derived from the travel-time and amplitude images, which is then used for fracture characterisation.

The acoustic tool measures multiple distances from the sensor to the borehole wall. To determine the borehole shape, the measured data (i.e. radius (r) and angle (θ)) are transferred to distance data (x, y). This gives the possibility to accurately detect the movement of the tool from its actual position to the centre of the borehole.

choosing the ellipse equation in the fitting model refers to the borehole geometry, in the ideal case when the stress around the borehole wall is equal in all directions, the borehole shape will be circular. However, when the borehole wall is compressed or elongated due to changes in the stress around the wall, the shape tends to be elliptical.

Then ellipse fitting process is performed using non-linear least square function to find the borehole dimension, optimising the squared sum of orthogonal distances from the distance point (x, y) to the fitted ellipse. The equation of the ellipse is that parametrised by $0 \leq \theta < 2\pi$ is giving by:

$$X(\theta) = X_0 + a\cos(\theta)\cos(\beta) - b\sin(\theta)\sin(\beta) \tag{5.1}$$

$$Y(\theta) = Y_0 + a\cos(\theta)\cos(\beta) + b\sin(\theta)\cos(\beta) \tag{5.2}$$

where β is the rotation angle, (X_0, Y_0) is the tool offset, a is the semi-major axis and b is semi-minor axis, ϕ is the tool rotation angle.

By fitting an ellipse to the unwrapped polar travel time co-ordinates, the values β, a, b, X_0 and Y_0 can be estimated. The sensor offset information is

particularly important as it allows to correct the travel time measurements and compensate this offset as well as correcting the dip and dip direction estimation.

While estimating these parameters allows a limited correction of the fracture geometry variables extracted from the unwrapped sine wave in the polar acoustic amplitude plot, they fail to account for the effects of borehole breakout or other irregular effects which could significantly distort the shape of the nominally-sinusoidal signature.

5.1.2 Fracture Detection and Characterisation in Deformed Borehole

Hough transform has been successfully used for the detection of sinusoidal response from planar fractures [18, 21], there does not appear any published resources dealing with sine waves with a degree of systematic distortion.

In order to characterise distorted fracture in deformed borehole geometry, a modified version of Equation 4.4 has been proposed as follows:

$$y = A\rho(\phi, y_0)\sin(\omega x + \theta) + y_0 \tag{5.3}$$

where A is the amplitude, y_0 is the baseline position of the sinusoid, θ is the phase and ω ($\omega = 2\pi/T$) is the angular frequency, T is the image width (or borehole circumference), $r(\phi, y_0)$ is the measured distance between imaging tool (at specific depth y_0 and rotation angle ϕ) and borehole wall, ρ is the ratio between $r(\phi, y_0)$ and the ellipse major axis a, and ϕ is the rotation angle of the acoustic tool. In borehole televiewer images, ω can be considered constant, and the fracture signature can therefore be characterised completely by specifying β, ϕ and $\rho(\phi, y_0)$.

The proposed approach for fracture detection has been tested on a variety of synthetic dataset, as shown in Figures 5.3(a) and 5.4(a), and the error between detected and expected dip angle (θ) is calculated.

As discussed earlier, the fracture depends on the borehole shape as clearly shown in Figures 5.3(b) and 5.4(b). While the use of conventional Hough transform can only detect an ideal sinusoid, this does not detect the actual fracture shape and its parameters, while the use of the proposed multi-channel approach can detect any distorted fracture as shown in Figure 5.5, provided the borehole wall has been adequately characterised by the acoustic travel-time measurements.

The error between detected and expected dip angle is calculated, in Figure 5.5(a), the error in the angle is 17°, while the error in Figure 5.5(b) is 8°. Using the proposed method reduces the error in both cases the angle to less than 1°, (this is using accumulator resolution of 100×100, as shown in Figure 4.3), which is comparable to the error expected from a perfect sine wave.

5.2   Multi-sensor Borehole Data

Data combination means combining information from several sources, in a sensible way, in order to estimate or predict some aspect of an observed scene, leading to the building of a world model of the environment. The term sensor fusion means the combination of sensory data or data derived from sensory data, such that the resulting information is better than it would be if these sensors were used individually [82–84].

Generally, the potential advantages of using multi-sensor data are listed be-
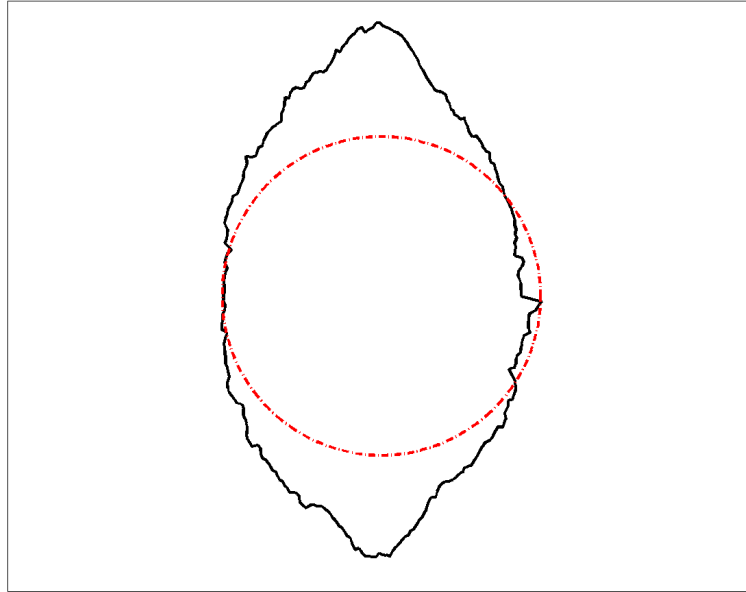
(a) Example 1: Distorted borehole shape
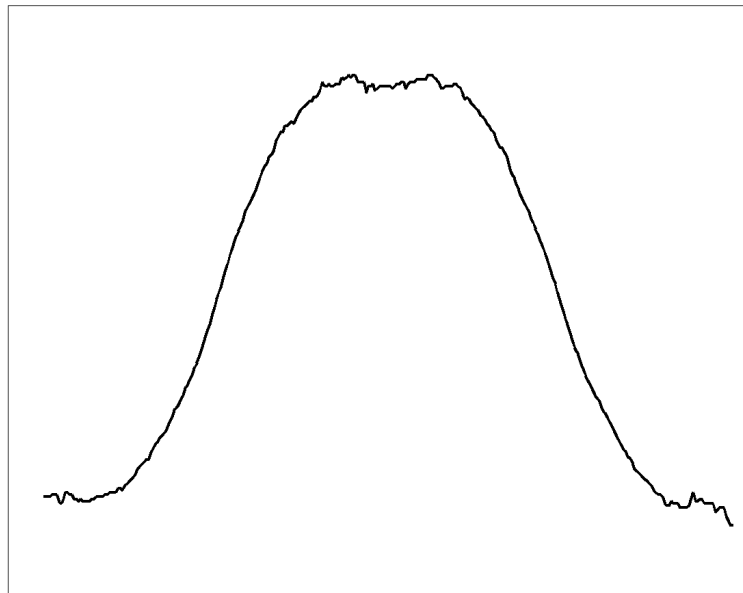
(b) Fracture shape in the Example 1

Figure 5.3: Example 1: Borehole shape and its fracture shape. The black line represents distorted borehole while the red line represents in-gauge borehole
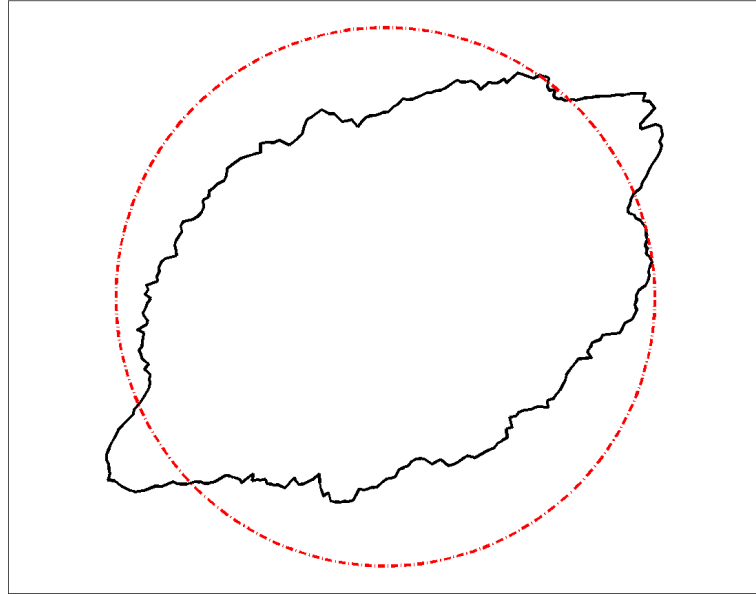
(a) Example 2: Distorted borehole shape
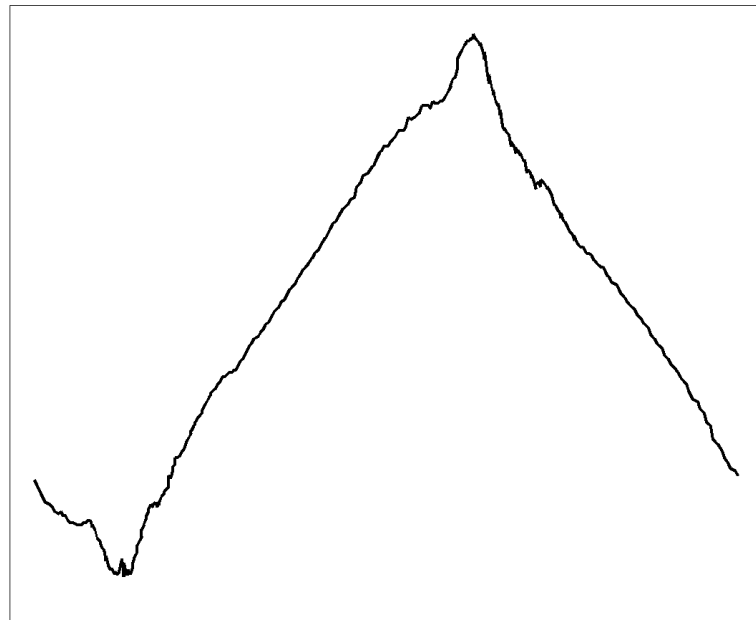
(b) Fracture shape in the Example 2

Figure 5.4: Example 2: Borehole shape and its fracture shape. The black line represents distorted borehole, while the red line represents in-gauge borehole
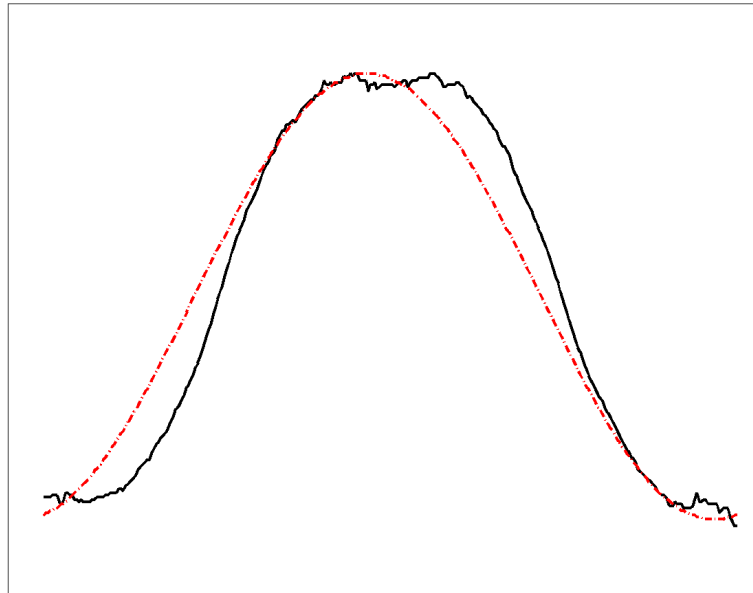
(a) Fracture detection result in Example 1
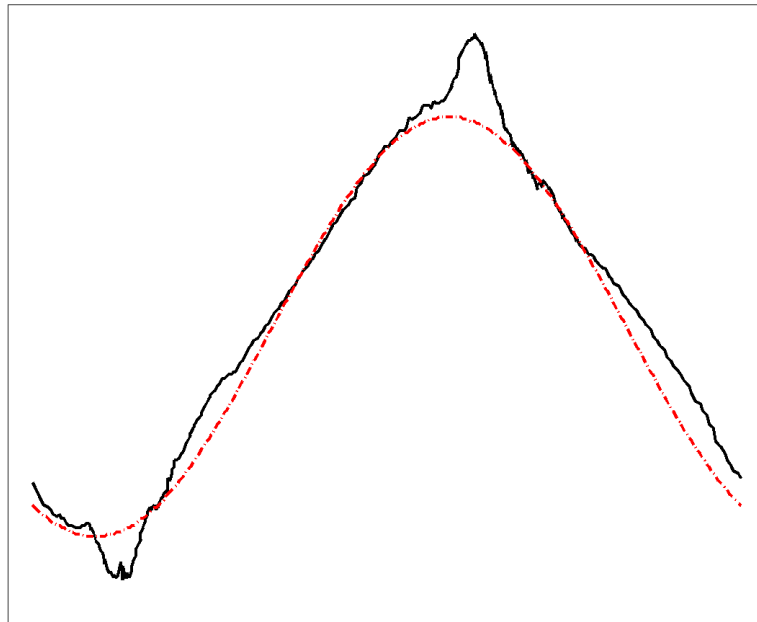
(b) Fracture detection result in Example 2

Figure 5.5: Fracture detection results in different borehole geometries. The black line represents detected fracture using proposed method, while the red line represents detected fracture using conventional Hough transform

low [85–87]:

(a) Multiple sensors would provide redundancy which, in turn, would enable the system to provide information in case of partial failure, data loss from one sensor i.e., fault tolerance capability robust functional and operational performance.

(b) One sensor can look where other sensors cannot look and provide observations enhanced spatial or geometrical coverage, and complementary information is made available.

(c) Measurements of one sensor are confirmed by the measurements of the other sensors, obtaining cooperative arrangement and enhancing the confidence increased confidence in the inferred results.

(d) Joint information would tend to reduce ambiguous interpretations and hence less uncertainty.

(e) Increased dimensionality of the measurement space, say measuring the desired quantity with optical sensors and ultrasonic sensors, the system is less vulnerable to interferences providing a sustained availability of the data.

(f) Multiple independent measurements when fused would improve the resolution enhanced spatial resolution.

(g) Improved detection of the objects because of less uncertainty provided by the fusion process.

Multi-sensor provide *redundant information* or *complementary information*. Redundant information is provided by a group of sensors (or a single sensor over time) when each sensor is perceiving, possibly with a different fidelity, the same features in the environment. The merge of redundant information can reduce

overall uncertainty and thus serve to increase accuracy. Complementary information from multiple sensors allows features in the environment to be perceived that are impossible to recognise using just the information from each individual sensor operating separately [88, 89].

The fundamental requirements, that can be identified for any image fusion system before other considerations, are [90–92]:

(a) The fused image should preserve (as far as possible) all salient information in the source images.

(b) The fusion process should not introduce any artefacts or inconsistencies into the fused image.

(c) Undesirable features in the source imagery (e.g. noise) should be suppressed in the fused image.

Multi-sensor fusion can occur at the pixel-level, feature-level or decision-level of representation. Pixel-level fusion generates a fused image in which each pixel is determined from a set of pixels in each source image. Feature-level fusion first employs feature extraction on the source data so that features from each source can be jointly employed for some purposes. Decision fusion combines decisions from several experts, i.e., based on voting [88, 93]. This research concentrate on feature fusion method to aggregate acoustic and optical borehole data to increase detection accuracy and reliability.

5.2.1 Multi-sensor Borehole Data Combination

The proposed method adopted here is based on using optical and acoustic (amplitude) borehole data for the same borehole to investigate the advantage of using multi-sensor data in terms of detection accuracy and system reliability. The pro-

posed method combines the extracted edge features from both borehole data to create new edge image, the general method framework is summarised as follows:

1. Fracture location alignment, each fracture in both borehole data should have the same location, this can be done by defining the fracture zone (between the first and last fracture in borehole data) and aligning all borehole data based on it.

2. Edge detection using the modified version of Canny edge detection to find fracture edge in each borehole data as described in section 4.2, as shown in Figures 5.6(b) and 5.7(b).

3. Combine extracted edges in one feature set using OR logical operator, as shown in Figure 5.8.

4. Edge processing by applying edge filtering followed by edge thinning to have a clear edge map.

5. Fracture characterisation using the modified Hough transform.

Figure 5.7(a), contains 11 fractures, as confirmed by Roberson Gelogging Ltd. geologists. By using single-sensor data, for optical borehole data detection result, only 6 fractures out of 11 are detected as shown in Figure 5.9(b), while for acoustic data, 8 fractures are detected as shown in Figure 5.9(a). The True Positive rate (TP i.e. which are correctly detected) for optical and acoustic data are 54.5% and 72.7% respectively. By using multi-sensor borehole data, the 11 fractures are detected as shown in Figure 5.9(c), the TP rate is increased by 45.5% and 27.3% for optical and acoustic data respectively (all fractures are detected).
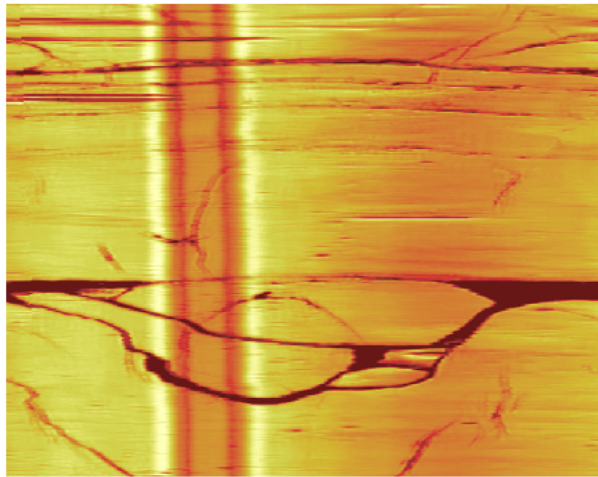
(a) Acoustic amplitude borehole data
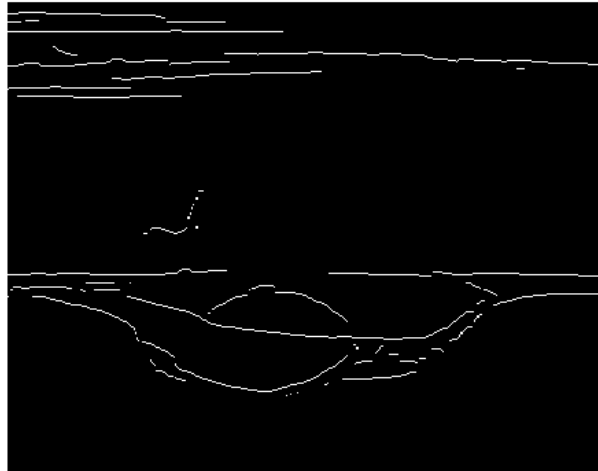
(b) Extracted Edge

Figure 5.6: Edge detection in acoustic amplitude borehole data

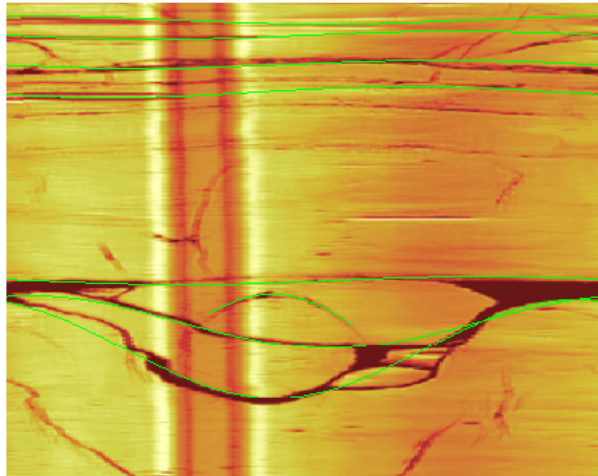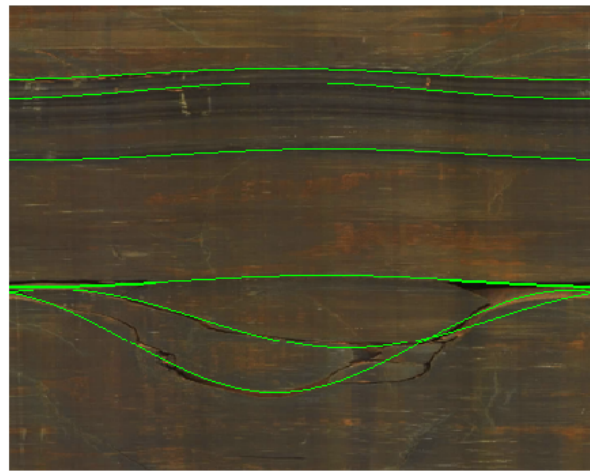(a) Optical borehole data

(b) Extracted Edge

Figure 5.7: Edge detection in optical borehole data

Figure 5.8: Combined extracted edges of optical and acoustic borehole data

(a) Acoustic fracture detection result

(b) Optical fracture detection result
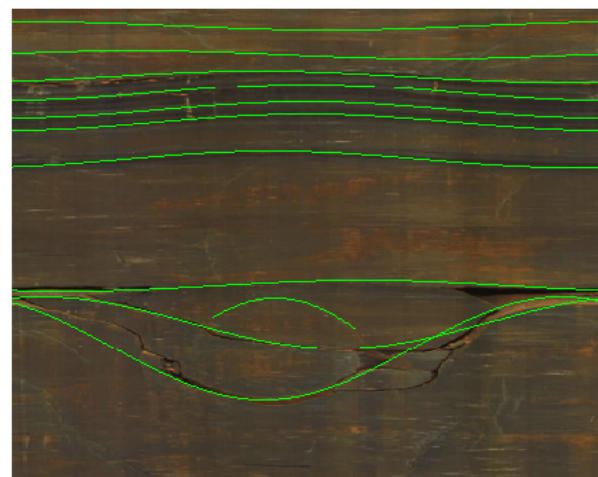
(c) Data fusion fracture detection result

Figure 5.9: Comparison of fracture detection between using data fusion and single borehole data

5.3   Summary

This chapter has proposed a new method for fracture detection and characterisation in acoustic borehole data. The proposed methods use the acoustic travel time data to find the actual borehole geometry. Then, non-linear least square ellipse fitting to find the borehole dimensions, knowing the borehole diameters can help to determine the stress direction around the borehole wall. The modified version of Hough transform is used to detect and characterise the distorted fracture. The most significant achievement of the proposed method compared to the existing methods is the unique ability to detect distorted fractures from an arbitrary-shaped borehole. In addition, the error of detected angle is minimised to less than $1°$.

Moreover, this chapter has presented multi-sensor borehole data combination, using optical and acoustic amplitude data. The concept of data combination is introduced to enhance fracture detection accuracy. Specifically, the extracted fracture edge from optical and acoustic borehole data are combined to form one feature set. The results shows that significant increase in fracture detection accuracy has been achieved by increasing the true positive rate in both borehole data.

Chapter 6

Conclusions and Future Work

This research has proposed novel and promising methods to aid in the automation of detection of characterisation of fractures in different borehole data types as part of a comprehensive computer-aided interpretation tool. The proposed methods accurately detect complete or partial sinusoidal waves in high noise images, in addition to cross-layer features and the phase shift between detected fractures, layers and veins/intrusions, which help geoscientist to study the stratigraphic and structural context. The most significant achievement of the proposed method compared to the existing methods is the unique ability to detect fractures and layers between layers or rocks that do not exhibit clear dark fracture edges, using unsupervised multi-resolution visual texture segmentation.

6.1 Conclusions

A complete automatic interpretation system has been developed to process borehole data. The system starts by pre-processing the borehole image as an essential stage to prepare the data for subsequent processing. The pre-processing procedures are data and background removal and decentralisation compensate, the use

of these methods have shown visual enhancement to the data, which is in favour of not only automatic interpretation but also manual interpretation by a human operator. Background removal are found to be well-suited when fractures are well separated from background noise, while affects on fractures part which overlaps with background noise. After borehole data is pre-processed, the data format suitable for further processing and fracture detection detection.

The next stage of fracture detection is image segmentation based on visual texture. Statistical and multi-resolution texture segmentation are presented as a tool for the discrimination of different types of rock layers, and various texture features are employed in order to automatically identify homogeneous image regions and find borehole fractures and layers. Feature extraction techniques are developed to extract those texture features most representative. It was shown that the combined statistical and multi-channel texture features proved to be suitable features for texture analysis.

The most computationally expensive stage of the borehole fracture detection process are defining number of clusters by using MH index and neural network, which thus acts as a bottleneck in the system. Neural networks were presented as a tool for pattern recognition and classification, and complete feature classification routines were detailed based on unsupervised neural networks.

For edge detection stage, modified Canny edge detection and skeletonisation methods have been adopted to find the boundaries from segmented image. It was shown that the methods performed well for edge detection and edge smoothing. However, smoothing stage of Canny edge affects on some segmented regions negatively.

The final stage of fracture detection is modified Hough transform for fracture characrisation. Using 2-D Hough transform instead of 3-D reduces computational time and memory requirement. In addition, the two attributes, i.e., *maximum pixel chain* and *maximum horizontal gap* with the accumulator magnitude eliminate false sinusoids that are detected due to the noise or intersection fractures. However, Hough transform is computationally expensive stage, which thus acts as a bottleneck in the system.

An intuitive GUI tool was built, offering many capabilities to the operator. The built GUI tool provides an output that is more readily understood by people not routinely involved in borehole data interpretation, and shows very good performance and user-friendliness. Automation of borehole data interpretation is a challenging task, yet not impossible. The tools presented in this work are not meant to replace human operators but rather help in minimising time, aiding in decision-making and reducing errors.

The research has proposed a new method for distorted fracture detection and characterisation in deformed borehole geometry. The proposed method uses the acoustic travel time data to find the actual borehole geometry, then non-linear least squares ellipse fitting to find the borehole dimension, knowing the borehole diameters can help to determine the stress direction around the borehole wall. The most significant achievement of the proposed method compared to the existing methods is the unique ability to detect distorted fractures from an arbitrary-shaped borehole. The proposed method is tested using synthetic data only, it needs to be verified using real borehole data.

Multi-sensor borehole data aggregation based has been introduced to enhance fracture detection accuracy. Specifically, the extracted fracture edge from optical

and acoustic borehole data are merged to form one feature set. The results show that significant increase of fracture detection accuracy has been achieved by increasing the true positive rate in both optical and acoustic borehole data. The proposed method would benefits from further using more data set.

6.2 Future Work

This study has presented several novel techniques for the processing of borehole data, several of which may be developed and refined further in order to increase their efficiency, robustness and speed of operation. In particular, the relative bottleneck caused by MH-index, neural network and modified Hough transform could be improved given a computationally viable alternative.

The proposed system performance could be enhanced by applying feature reduction and feature selection techniques on visual texture features to find the optimal feature set for borehole data discrimination. Finding the optimal features reduces system computational time. In addition, apply different classification and clustering methods and compare their results in terms of accuracy and efficiency.

Enhancing the automatic interpretation tool by adding several features according to industrial need, the examples of recommended features are as follows:

(i) Rock classification: This can be achieved by using supervised neural network in the proposed method to discernment rock different rock types.

(ii) Enhancing output representation: This can be achieved by providing recommendations to the geologists (e.g. borehole stability).

(iii) Representing results of the interpretation and borehole fracture in 3-D.

(iv) Commercial implementation of an automatic interpreter. This can be achieved by implementing the final system in a stand-alone robust software form for an on-site use on a standard portable computer device.

Bibliography

[1] T. Reid and J. Harrison, "A semi-automated methodology for discontinuity trace detection in digital images of rock mass exposures," *International Journal of Rock Mechanics and Mining Sciences*, vol. 37, no. 7, pp. 1073–1089, 2000.

[2] D. Ask and R. Christiansson, "Detection of borehole breakouts at the forsmark site, sweden," *Managing Indoor Air Quality*, p. 79, 2011.

[3] *Hi-OPTV Optical Televiewer Operating Manual*, Robertson Geologging Ltd, Deganwy Conwy, LL31 9PX, UK, 2014.

[4] *High resolution acoustic televiewer*, Robertson Geologging Ltd, Deganwy Conwy, LL31 9PX, UK, 2014.

[5] W. Al-Nuaimy, "Automatic feature detection and interpretation in groundpenetrating radar data." Ph.D. dissertation, University of Liverpool, 1999.

[6] K.-L. Du, "Clustering: A neural network approach," *Neural Networks*, vol. 23, no. 1, pp. 89–107, 2010.

[7] D. Gough and J. Bell, "Stress orientations from oil-well fractures in Alberta and Texas," *Canadian Journal of Earth Sciences*, vol. 18, no. 3, pp. 638–645, 1981.

[8] D. Ask and M. Ask, "Detection of potential borehole breakouts in boreholes kfm01a and kfm01b," *SKB P-report in prep*, 2006.

[9] W. Al-Sit, W. Al-Nuaimy, M. Marelli, and A. Al-Ataby, "Visual texture for automated characterisation of geological features in borehole televiewer imagery," *Journal of Applied Geophysics*, vol. 119, no. 0, pp. 139 – 146, 2015.

[10] J. Bell and D. Gough, "Northeast-southwest compressive stress in Alberta evidence from oil wells," *Earth and Planetary Science Letters*, vol. 45, no. 2, pp. 475–482, 1979.

[11] G. Kirsch, *Die theorie der elastizität und die bedürfnisse der festigkeitslehre.* Springer, 1898.

[12] H. A. Khair, D. Cooke, and M. Hand, "Seismic mapping and geomechanical analyses of faults within deep hot granites, a workflow for enhanced geothermal system projects," *Geothermics*, vol. 53, pp. 46–56, 2015.

[13] A. Zang, O. Stephansson, O. Heidbach, and S. Janouschkowetz, "World stress map database as a resource for rock mechanics and rock engineering," *Geotechnical and Geological Engineering*, vol. 30, no. 3, pp. 625–646, 2012.

[14] D. Moos and M. D. Zoback, "Utilization of observations of well bore failure to constrain the orientation and magnitude of crustal stresses: application to continental, deep sea drilling project, and ocean drilling program boreholes," *Journal of Geophysical Research: Solid Earth (1978–2012)*, vol. 95, no. B6, pp. 9305–9325, 1990.

[15] W. Meng, Q. Chen, Z. Zhao, M. Wu, X. Qin, and C. Zhang, "Characteristics and implications of the stress state in the Longmen Shan fault zone, eastern margin of the Tibetan Plateau," *Tectonophysics*, 2015.

[16] B. S. Aadnoy, J. S. Bell *et al.*, "Classification of drilling-induced fractures and their relationship to in-situ stress directions," *The Log Analyst*, vol. 39, no. 06, 1998.

[17] G. Y. Kim and B. Narantsetseg, "Fractures and breakouts analysis from borehole image logs: Preliminary results for interpretation of stress history and in situ stress state," *Marine Georesources & Geotechnology*, no. just-accepted, 2014.

[18] B. B. Thapa, P. Hughett, and K. Karasaki, "Semi-automatic analysis of rock fracture orientations from borehole wall images," *Geophysics*, vol. 62, no. 1, pp. 129–137, 1997.

[19] R. N. Anderson, "Methods for monitoring temperature-vs-depth characteristics in a borehole during and after hydraulic fracture treatments," May 23 1989, uS Patent 4,832,121.

[20] K. Glossop, P. Lisboa, P. Russell, A. Siddans, and G. Jones, "An implementation of the Hough transformation for the identification and labelling of fixed period sinusoidal curves," *Computer Vision and Image Understanding*, vol. 74, no. 1, pp. 96–100, 1999.

[21] Z. Changchun and S. Ge, "A Hough transform-based method for fast detection of fixed period sinusoidal curves in images," in *Signal Processing, 2002 6th International Conference on*, vol. 1. IEEE, 2002, pp. 909–912.

[22] T. Malone, B. Hubbard, D. Merton-Lyn, P. Worthington, and R. Zwiggelaar, "Borehole and ice feature annotation tool (bifat): A program for the automatic and manual annotation of glacier borehole images," *Computers & Geosciences*, vol. 51, pp. 381–389, 2013.

[23] C. He and W. Wang, "A PCNN-based edge detection algorithm for rock fracture images," in *Photonics and Optoelectronic (SOPO), 2010 Symposium on*. IEEE, 2010, pp. 1–4.

[24] W. Wang, H. Liao, and Y. Huang, "Rock fracture tracing based on image processing and SVM," in *Natural Computation, 2007. ICNC 2007. Third International Conference on*, vol. 1. IEEE, 2007, pp. 632–635.

[25] M. Johansson, "Digital image processing of borehole images for determination of rock fracture orientation and aperture," 1999.

[26] M. V. Ginkel, M. A. Kraaijveld, L. J. V. Vliet, E. P. Reding, P. W. Verbeek, and H. J. Lammers, "Robust curve detection using a Radon transform in orientation space applied to fracture detection in borehole images," in *ICCV2001*, 2001.

[27] S. Assous, P. Elkington, S. Clark, and J. Whetton, "Automated detection of planar geologic features in borehole images," *Geophysics*, vol. 79, no. 1, pp. D11–D19, 2013.

[28] J.-L. Deltombe and R. Schepers, "Combined processing of BHTV travel time and amplitude images," in *Proceedings from the Seventh International Symposium on Minerals and Geotechnical Logging, golden, Colorado, October*, 2000, pp. 24–26.

[29] N. Saito, N. N. Bennett, and R. Burridge, "Method of determining dips and azimuths of fractures from borehole images," Sep. 28 1999, uS Patent 5,960,371.

[30] M. A. Proett, T. J. Perkins, and R. Stamm, "Automatic anisotropy, azimuth and dip determination from upscaled image log data," Dec. 24 2013, US Patent 8,614,577.

[31] P. Gaillot, T. Brewer, P. Pezard, and Y. En Chao, "borehole imaging tools-principles and applications," *Scientific Drilling*, no. 5, pp. 1–4, 2007.

[32] D. Evans, A. Kingdon, E. Hough, W. Reynolds, and N. Heitmann, "First account of resistivity borehole micro-imaging (FMI) to assess the sedimentology and structure of the Preesall Halite, New England: implications for gas storage and wider applications in CCS caprock assessment," *Journal of the Geological Society*, vol. 169, no. 5, pp. 587–592, 2012.

[33] R. Geologging, *Micro-Resistivity Imaging Probes*, 2014 (accessed October 19, 2014), http://www.geologging.com/wp-content/uploads/2014/05/Micro-resistivity-Imaging-Probe.pdf.

[34] M. Tuceryan and A. K. Jain, "Texture analysis," *The Handbook of Pattern Recognition and Computer Vision*, vol. 2, pp. 207–248, 1998.

[35] C. Chen, "Handbook of Pattern Recognition and Computer Vision," 2010.

[36] J. M. Coggins, "A framework for texture analysis based on spatial filtering," 1983.

[37] S. Brahnam, L. C. Jain, A. Lumini, and L. Nanni, "Introduction to local binary patterns: New variants and applications," in *Local Binary Patterns: New Variants and Applications*. Springer, 2014, pp. 1–13.

[38] J. Sklansky, "Image segmentation and feature extraction," *Systems, Man and Cybernetics, IEEE Transactions on*, vol. 8, no. 4, pp. 237–247, 1978.

[39] R. M. Haralick, "Statistical and structural approaches to texture," *Proceedings of the IEEE*, vol. 67, no. 5, pp. 786–804, 1979.

[40] A. R. Rao, *A taxonomy for texture description and identification*. Springer Publishing Company, Incorporated, 2012.

[41] C. K. Chui, *Wavelets: a tutorial in theory and applications*. Academic Press, 2012, vol. 2.

[42] K. Chaurasia and P. Garg, "A brief review on texture analysis methods," *Studies in Surveying and Mapping Science*, vol. 1, no. 2, 2013.

[43] R. M. Haralick, K. Shanmugam, and I. H. Dinstein, "Textural features for image classification," *Systems, Man and Cybernetics, IEEE Transactions on*, no. 6, pp. 610–621, 1973.

[44] I. Daubechies, "Orthonormal bases of compactly supported wavelets," *Communications on Pure and Applied Mthematics*, vol. 41, no. 7, pp. 909–996, 1988.

[45] M. Misiti, Y. Misiti, G. Oppenheim, and J.-M. Poggi, *Wavelets and their Applications.* John Wiley & Sons, 2013.

[46] T. Ojala and M. Pietikäinen, "Texture classification," *CVonline: The Evolving, Distributed, Non-Proprietary, On-Line Compendium of Computer Vision*, 2001.

[47] B. Julesz, "Visual pattern discrimination," *Information Theory, IRE Transactions on*, vol. 8, no. 2, pp. 84–92, 1962.

[48] A. Gallace and C. Spence, *In touch with the future: The sense of touch from cognitive neuroscience to virtual reality.* Oxford University Press, 2014.

[49] B. Julesz, *Nonlinear and cooperative processes in texture perception.* MIT Press, Cambridge, MA, 1981.

[50] ——, "A theory of preattentive texture discrimination based on first-order statistics of textons," *Biological Cybernetics*, vol. 41, no. 2, pp. 131–138, 1981.

[51] R. W. Conners and C. A. Harlow, "A theoretical comparison of texture algorithms," *Pattern Analysis and Machine Intelligence, IEEE Transactions on*, no. 3, pp. 204–222, 1980.

[52] R. T. Elunai, "Particulate texture image analysis with applications," 2011.

[53] P. P. Ohanian and R. C. Dubes, "Performance evaluation for four classes of textural features," *Pattern Recognition*, vol. 25, no. 8, pp. 819–833, 1992.

[54] A. Fernández, M. X. Álvarez, and F. Bianconi, "Texture description through histograms of equivalent patterns," *Journal of Mathematical Imaging and Vision*, vol. 45, no. 1, pp. 76–102, 2013.

[55] A. Abutaleb and A. Eloteifi, "Automatic thresholding of gray-level pictures using 2-d entropy," in *31st Annual Technical Symposium*. International Society for Optics and Photonics, 1988, pp. 29–35.

[56] A. Brink, "Thresholding of digital images using two-dimensional entropies," *Pattern Recognition*, vol. 25, no. 8, pp. 803–808, 1992.

[57] R. L. De Valois, D. G. Albrecht, and L. G. Thorell, "Spatial frequency selectivity of cells in macaque visual cortex," *Vision Research*, vol. 22, no. 5, pp. 545–559, 1982.

[58] J. Schmidhuber, "Deep learning in neural networks: An overview," *Neural Networks*, vol. 61, pp. 85–117, 2015.

[59] S. Marčelja, "Mathematical description of the responses of simple cortical cells," *JOSA*, vol. 70, no. 11, pp. 1297–1300, 1980.

[60] H. Strasburger, I. Rentschler, and M. Jüttner, "Peripheral vision and pattern recognition: A review," *Journal of Vision*, vol. 11, no. 5, p. 13, 2011.

[61] T. R. Reed and H. Wechsler, "Segmentation of textured images and gestalt organization using spatial/spatial-frequency representations," *Pattern Analysis and Machine Intelligence, IEEE Transactions on*, vol. 12, no. 1, pp. 1–12, 1990.

[62] A. K. Jain and F. Farrokhnia, "Unsupervised texture segmentation using Gabor filters," in *Systems, Man and Cybernetics, 1990. Conference Proceedings., IEEE International Conference on.* IEEE, 1990, pp. 14–19.

[63] L. Stankovic, M. Daković, and T. Thayaparan, *Time-frequency signal analysis with applications.* Artech House, 2013.

[64] A. K. Jain and R. Dubes, "Feature definition in pattern recognition with small sample size," *Pattern Recognition*, vol. 10, no. 2, pp. 85–97, 1978.

[65] J. B. W. G. Biswas, "Conceptual clustering with systematic missing values," in *Machine Learning Proceedings 1992: Proceedings of the Ninth International Workshop (ML92).* Morgan Kaufmann, 2014, p. 464.

[66] T. P. Weldon, W. E. Higgins, and D. F. Dunn, "Efficient Gabor filter design for texture segmentation," *Pattern Recognition*, vol. 29, no. 12, pp. 2005–2015, 1996.

[67] R. C. Dubes, "How many clusters are best?-an experiment," *Pattern Recognition*, vol. 20, no. 6, pp. 645–663, 1987.

[68] O. Arbelaitz, I. Gurrutxaga, J. Muguerza, J. M. Pérez, and I. Perona, "An extensive comparative study of cluster validity indices," *Pattern Recognition*, vol. 46, no. 1, pp. 243–256, 2013.

[69] J. Carlis and K. Bruso, "Rsqrt: An heuristic for estimating the number of clusters to report," *Electronic commerce research and applications*, vol. 11, no. 2, pp. 152–158, 2012.

[70] L. Hubert and J. Schultz, "Quadratic assignment as a general data analysis strategy," *British Journal of Mathematical and Statistical Psychology*, vol. 29, no. 2, pp. 190–241, 1976.

[71] B. F. Manly, *Randomization, bootstrap and Monte Carlo methods in biology*. CRC Press, 2006, vol. 70.

[72] D. W. Patterson, *Artificial neural networks: theory and applications*. Prentice Hall PTR, 1998.

[73] L. I. Kuncheva, *Combining pattern classifiers: methods and algorithms*. John Wiley & Sons, 2004.

[74] J. M. Zurada, "Introduction to artificial neural systems," 1999.

[75] T. Heimann and H.-P. Meinzer, "Statistical shape models for 3d medical image segmentation: a review," *Medical Image Analysis*, vol. 13, no. 4, pp. 543–563, 2009.

[76] M. Oskoei and H. Hu, "A survey on edge detection methods," Technical Report: CES-506. University of Essex, Tech. Rep., 2010.

[77] J. Canny, "Finding edges and lines in images," *Massachusetts Inst. of Tech. Report*, vol. 1, 1983.

[78] ——, "A computational approach to edge detection," *Pattern Analysis and Machine Intelligence, IEEE Transactions on*, no. 6, pp. 679–698, 1986.

[79] S. Ansari, S. Prabhu, G. N. Kini, G. Hegde, and Y. Haider, "A survey on conventional edge detection techniques," *International Journal of Scientific Research in Computer Science Applications and Management Studies*, vol. 3, no. 1, 2014.

[80] J. Illingworth and J. Kittler, "A survey of the Hough transform," *Computer vision, graphics, and image processing*, vol. 44, no. 1, pp. 87–116, 1988.

[81] P. Mukhopadhyay and B. B. Chaudhuri, "A survey of Hough transform," *Pattern Recognition*, vol. 48, no. 3, pp. 993–1010, 2015.

[82] J. R. Raol, *Multi-Sensor Data Fusion with MATLAB®*.   CRC Press, 2009.

[83] D. Tansky, A. Fischer, B. M. Colosimo, L. Pagani, and Y. B. Shabat, "Multi-sensor multi-resolution data fusion modeling," *Procedia CIRP*, vol. 21, pp. 151–158, 2014.

[84] V. Petrovic and T. Cootes, "Information representation for image fusion evaluation," in *Information Fusion, 2006 9th International Conference on.* IEEE, 2006, pp. 1–7.

[85] J. R. Raol, G. Girija, and J. Singh, *Modelling and parameter estimation of dynamic systems.*   IET, 2004, vol. 65.

[86] R. C. Eberhart and R. W. Dobbins, *Neural network PC tools: a Practical Guide.*   Academic Press Professional, Inc., 1990.

[87] R. C. Luo, C.-C. Yih, and K. L. Su, "Multisensor fusion and integration: approaches, applications, and future research directions," *Sensors Journal, IEEE*, vol. 2, no. 2, pp. 107–119, 2002.

[88] R. S. Blum and Z. Liu, *Multi-sensor image fusion and its applications.*   CRC press, 2005.

[89] D. Hall and J. Llinas, *Multisensor data fusion.*   CRC press, 2001.

[90] M. I. Smith and J. P. Heather, "A review of image fusion technology in 2005," in *Defense and Security.*   International Society for Optics and Photonics, 2005, pp. 29–45.

[91] B. Khaleghi, A. Khamis, F. O. Karray, and S. N. Razavi, "Multisensor data fusion: A review of the state-of-the-art," *Information Fusion*, vol. 14, no. 1, pp. 28–44, 2013.

[92] A. Toet, M. A. Hogervorst, S. G. Nikolov, J. J. Lewis, T. D. Dixon, D. R. Bull, and C. N. Canagarajah, "Towards cognitive image fusion," *Information fusion*, vol. 11, no. 2, pp. 95–113, 2010.

[93] R. S. Blum, "On multisensor image fusion performance limits from an estimation theory perspective," *Information Fusion*, vol. 7, no. 3, pp. 250–263, 2006.

Appendix A

Fracture Detection Results

A.1 Acoustic Borehole Fracture Detection Results

This section presents results for acoustic borehole data as shown Figure A.1. It was found and verified by expert geophysicists interpretation, that automatic annotation correctly labels all the rock fractures, with a (1%) false positive rate.
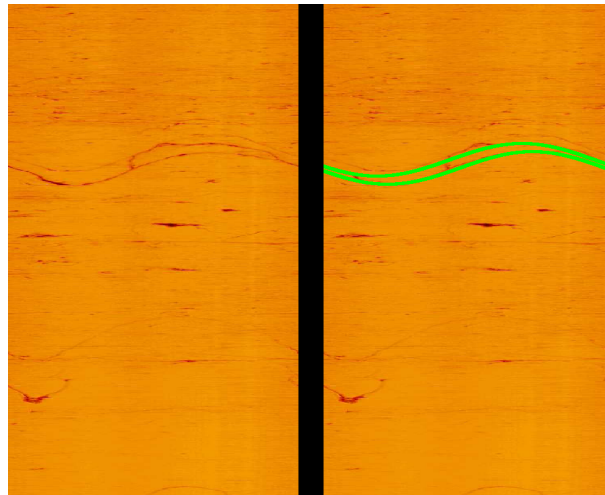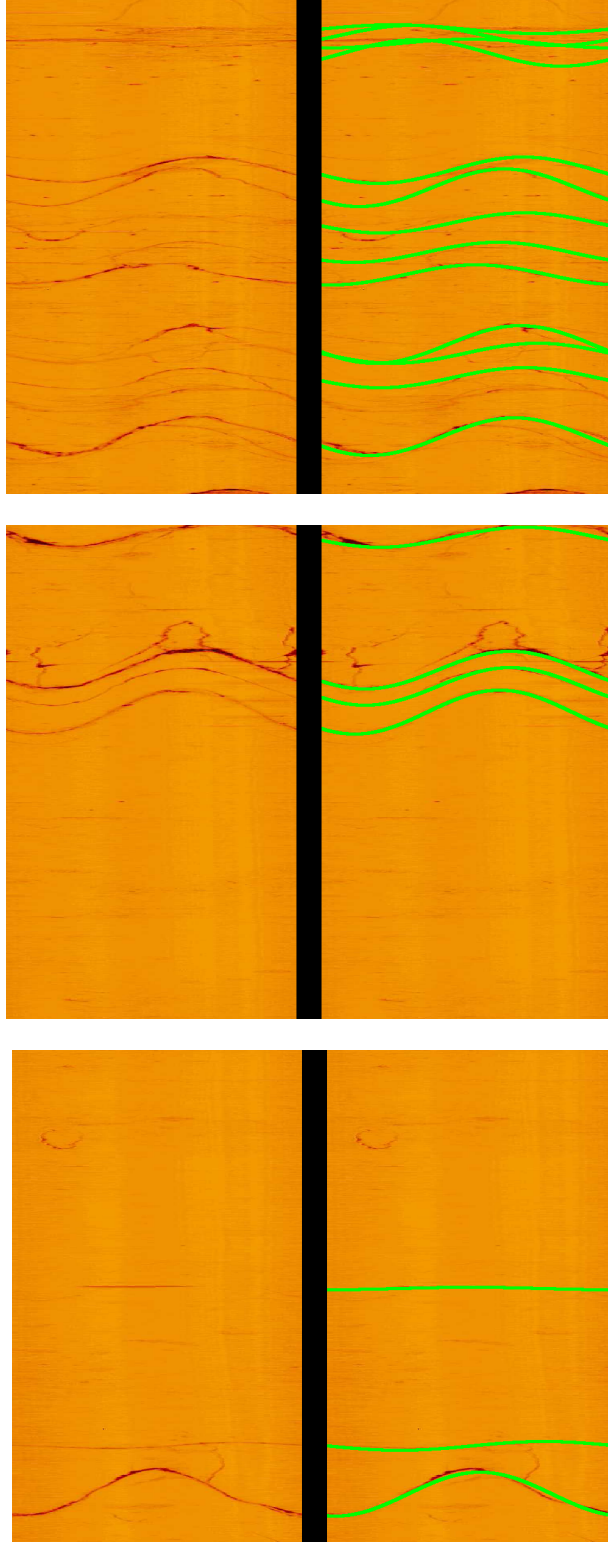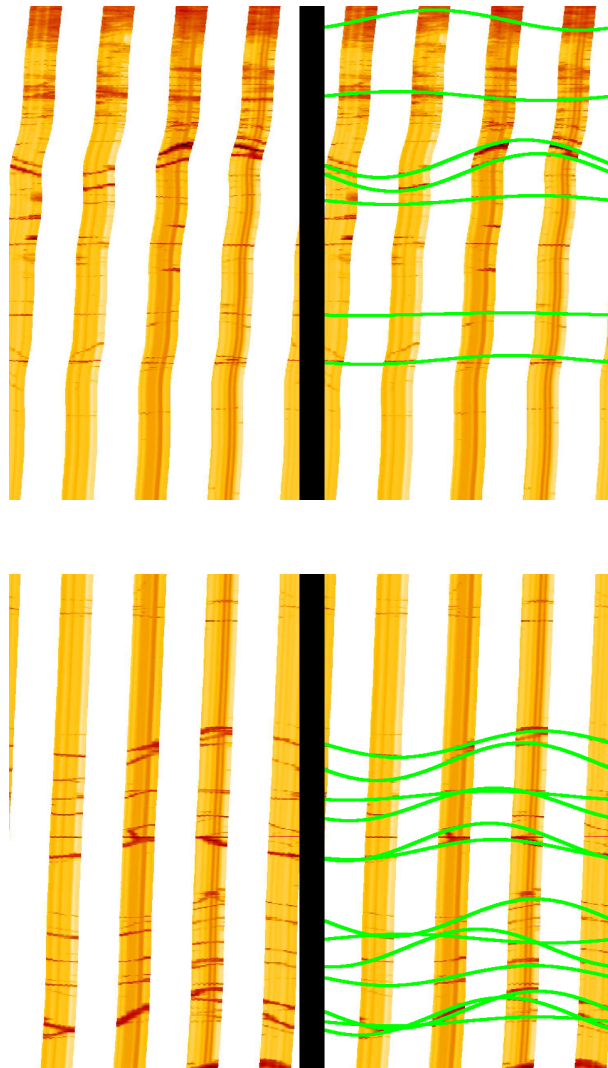
Figure A.1: Acoustic borehole data detection result

A.2 Resistivity Borehole Fracture Detection Results

This section presents results for resistivity borehole data as shown Figure A.2. It was found and verified by expert geophysicists interpretation, that automatic annotation correctly labels all the rock fractures, with a (1%) false positive rate.
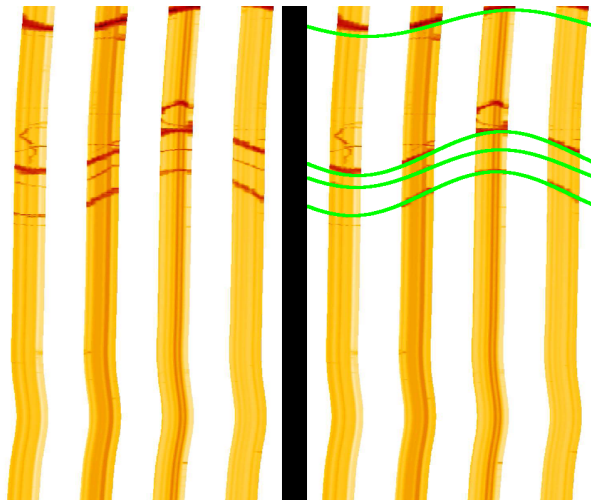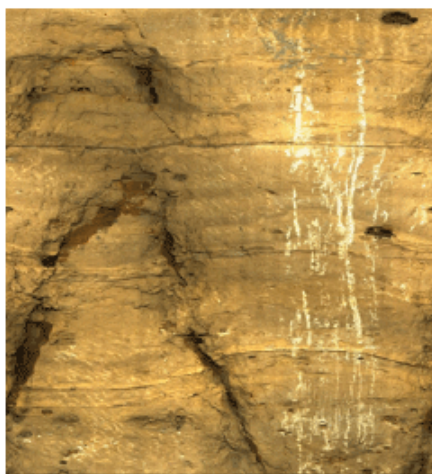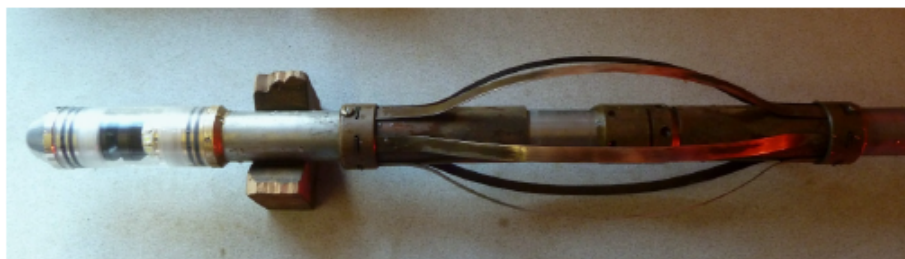
Figure A.2: Resistivity borehole data detection result

Appendix B

Optical Televiewer Specifications

ROBERTSON GEOLOGGING LIMITED

Robertson Geologging

Hi-OPTV Optical Televiewer
Operating Manual

Rev: October 2013

Robertson Geologging Ltd
Deganwy, Conwy
LL31 9PX

1 - PACKING LIST

P/N code	Description
I002180	**Hi-OPTV probe (standard, at 10 MPa).** Includes OPTV dedicated acquisition software (on a CD) and Emind logger
I013916	**Hi-OPTV probe with "natural gamma" (10 Mpa).** Includes OPTV acquisition software (on a CD) and Emind logger
I013758	**Hi-OPTV probe (standard, at 20 MPa).** Includes OPTV acquisition software (on a CD) and Emind logger
I013917	**Hi-OPTV probe with "natural gamma" (20 Mpa).** Includes OPTV acquisition software (on a CD) and Emind logger
I014358	**Hi-OPTV image alignment calibration jig**
I015464	**Natural Gamma test blanket**
I001691	42 mm **Non-magnetic Centralisers** (70 – 110 mm range) – 2 required
I001692	42 mm **Non-magnetic Centralisers** (90 – 180 mm range) – 2 required
I001693	42 mm **Non-magnetic Centralisers** (180 – 260 mm range) – 2 required
I001694	42 mm **Non-magnetic Centralisers** (260 – 342 mm range) – 2 required
I001695	42 mm **Non-magnetic Centralisers** (342 – 472 mm range) – 2 required
I001801	**Locking collars** for centralizer – 4 required
I000460	**RGLDip** Imaging and processing software (with USB key)

2 - PROBE PHYSICAL SPECIFICATIONS

- Diameter   52 mm or 61 mm (depending on pressure range)
- Length   1.63 m
- Temperature rating   0 – 60°C
- Pressure range   0-10 MPa (0-20 MPa for extended range version)
- Weight   5 kg
- Sampling rate   user selectable (20 to 60 pictures per second)
- Sensor Type   1280x1024 pixels (CMOS image sensor)
- Azimuthal resolution   360, 720, 900, 1080, 1260, 1440 pixels per revolution
- Vertical resolution   function of winch speed
- Colour resolution   24 bit RGB
- Optic   360 degrees circular view lens, (0 to infinite focus)
- Light and exposure   user selectable
- Orientation device   3 axis magnetometers and 3 accelerometers (inclination accuracy: ±0.5 degree, azimuth accuracy: ±1.0 degree)
- Surface Power   90-110 V
- Supported cable type   mono or 4 conductors
- Borehole diameter range   75 to 470 mm (depending on borehole conditions)
- Borehole conditions   water or air-filled (muddy fluid or fragments can affect data quality)

- Casing   open hole or PVC case (steel case will alter magnetic orientation system)
- Logging speed   depending on desired resolution, winch type and borehole diameter (from 1 to 10 meter/minute)
- Centralization   2 centralizers with locking collars required

Sensors	Offsets (from tool bottom)
Center of the optic window	8 cm
Natural Gamma (OPTIONAL)	145 cm

SAFETY NOTICE

This equipment is energised at up to 120 Volts by the surface system. Ensure that the sonde power is switched off before attaching or detaching the logging cable. Hazardous voltages (up to 2 kV) may be present inside this equipment when powered from the surface system.

3 - SYSTEM OVERVIEW

Hi-OPTV (Optical Televiewer) provides a continuous very high resolution oriented 360° image of the borehole sidewall using conventional LEDs lights source and a unique optical system based on a fisheye lens.
The information is processed in real time to produce a complete 'unwrapped' real colour image perpendicularly to the tool (borehole) axis.
The probe can operate also in air-filled boreholes although it is unsuitable for boreholes containing dense muds or cloudy fluids.
Its output can be easily combined with HRAT results in RGLDip software generally offering superior resolution to the acoustic probe in term of layers definitions.

OPTV applications include:

- Fracture identification and orientation (local stress studies)
- Stratigraphic studies (even very thin layers detection)
- Lithology characterization
- Core orientation and borehole deviation studies
- Casing studies

RGLDip, the RG image interpretation software package, offers manual and automatic feature recognition options to define their orientations (dip/strike and azimuth) and that of the borehole.
Display options include stereographic projections of zone axes, orientation frequency plots and "synthetic cores" for comparison with real core data.

Appendix C

The Automatic Interpretation Tool

The unavailability of commercial software for automatic fracture detection and characterisation that helps the operator to detect and characterise fractures makes manual interpretation is the only solution. This interpretation is therefore prone to human error and a time consuming process. One of the important and valuable outputs of this research is an interpretation tool that is very convenient to the operators. In contrast to the manual interpretation, the developed tool provides automatic interpretation results in a user-friendly GUI environment that offers many capabilities. It has been implemented using MATLAB GUIDE tool in order to facilitate executing the developed algorithms (MATLAB functions). The tool has a main GUI that shows the available options (as shown in Figure C.1). These options are:

(a) Borehole data segmentation.

(b) Background removal

(c) Various options of edge detection (i.e. Canny and gradient).
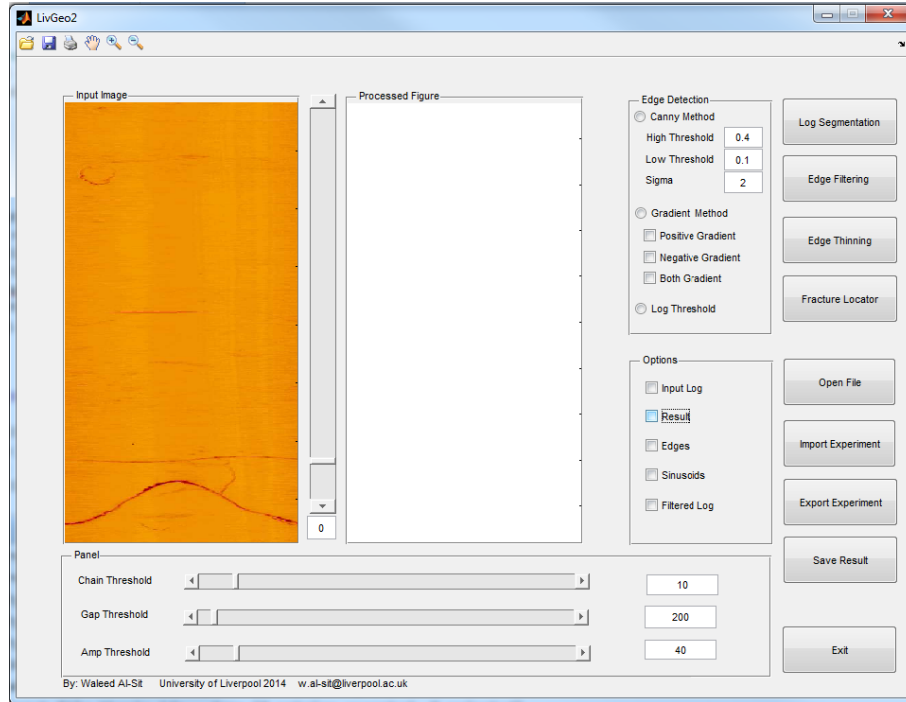
(d) Edge filtering and thinning.

Figure C.1: GUI tool main menu

(e) Thresholding.

(f) Fracture detection.

Figures C.2 to C.4 show the result of executing the options of the tool (namely, edge detection, synthetic result, Fracture detection and characterisation). Besides this option, the GUI are equipped with facilities like load, save, export and import.

The built GUI tool provides an output that is more readily understood by people not routinely involved in borehole fracture detection, and remarkable performance and user-friendliness. Other options and capabilities can be added to the GUI easily in the future according to operator recommendations.
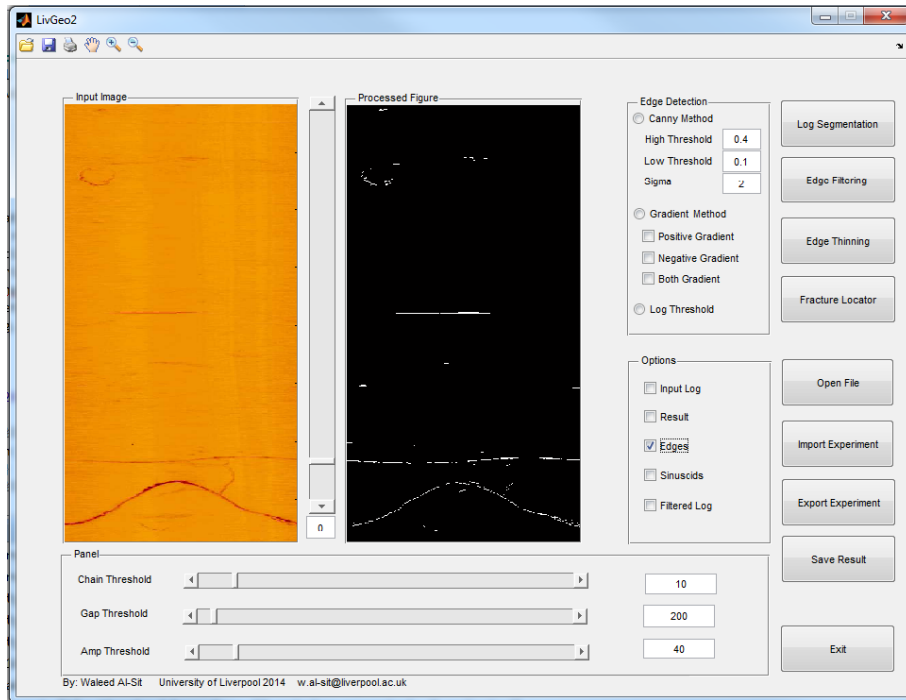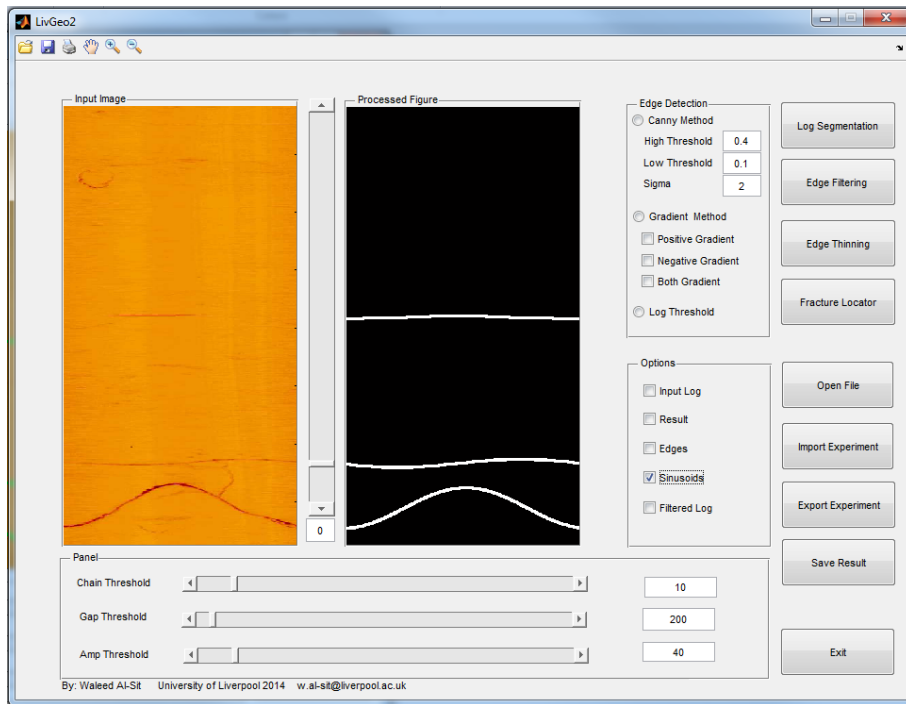
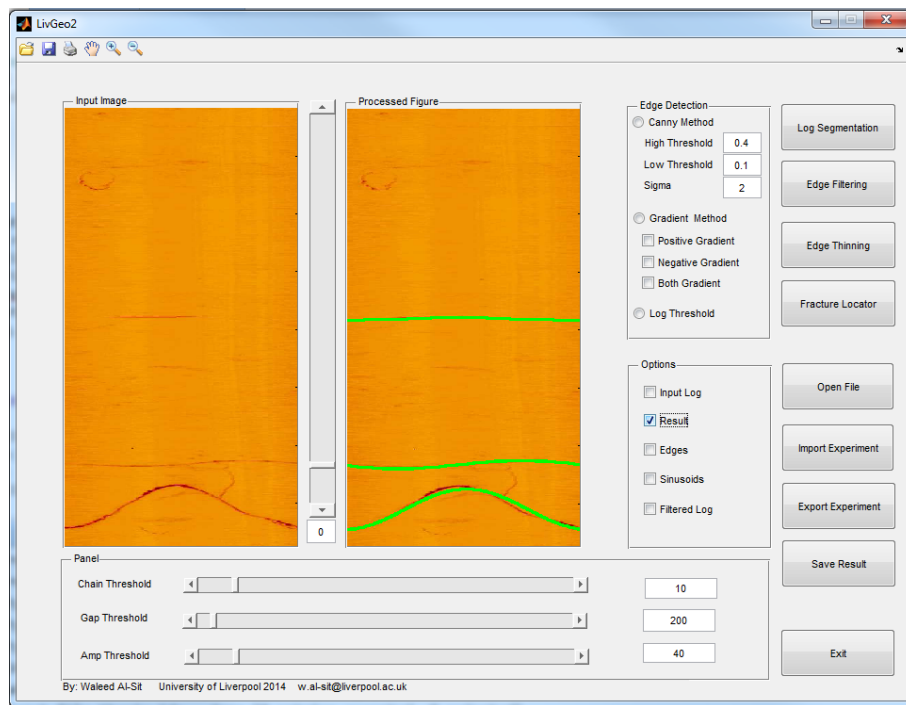Figure C.2: Edge detection processing window

Figure C.3: Synthetic result window

Figure C.4: Fracture detection and characterisation processing window